JCB Journal of Cell Biology

ARTICLE

The E3 ligase TRIM1 ubiquitinates LRRK2 and controls its localization, degradation, and toxicity

Adrienne E.D. Stormo[1], Farbod Shavarebi[19], Molly FitzGibbon[19]*, Elizabeth M. Earley[1]*, Hannah Ahrendt[19]*, Lotus S. Lum[1], Erik Verschueren[2,6], Danielle L. Swaney[2,6], Gaia Skibinski[7,8], Abinaya Ravisankar[7,8], Jeffrey van Haren[3,9], Emily J. Davis[1], Jeffrey R. Johnson[2,6], John Von Dollen[2,6], Carson Balen[19], Jacob Porath[19], Claudia Crosio[11], Christian Mirescu[10], Ciro Iaccarino[11], William T. Dauer[12,13,14], R. Jeremy Nichols[15], Torsten Wittmann[3], Timothy C. Cox[16,17], Steve Finkbeiner[4,5,7,8], Nevan J. Krogan[2,6,8], Scott A. Oakes[1,18], and Annie Hiniker[19]

Missense mutations in leucine-rich repeat kinase 2 (LRRK2) are the most common cause of familial Parkinson's disease (PD); however, pathways regulating LRRK2 subcellular localization, function, and turnover are not fully defined. We performed quantitative mass spectrometry–based interactome studies to identify 48 novel LRRK2 interactors, including the microtubule-associated E3 ubiquitin ligase TRIM1 (tripartite motif family 1). TRIM1 recruits LRRK2 to the microtubule cytoskeleton for ubiquitination and proteasomal degradation by binding $LRRK2_{911–919}$, a nine amino acid segment within a flexible interdomain region ($LRRK2_{853–981}$), which we designate the "regulatory loop" (RL). Phosphorylation of LRRK2 Ser910/Ser935 within LRRK2 RL influences LRRK2's association with cytoplasmic 14-3-3 versus microtubule-bound TRIM1. Association with TRIM1 modulates LRRK2's interaction with Rab29 and prevents upregulation of LRRK2 kinase activity by Rab29 in an E3-ligase–dependent manner. Finally, TRIM1 rescues neurite outgrowth deficits caused by PD-driving mutant LRRK2 G2019S. Our data suggest that TRIM1 is a critical regulator of LRRK2, controlling its degradation, localization, binding partners, kinase activity, and cytotoxicity.

Introduction

Leucine-rich repeat kinase 2 (LRRK2) mutations are the most common genetic cause of Parkinson's disease (PD), a devastating neurodegenerative disorder affecting 1–2% of people >65 yr old (Klein and Westenberger, 2012; Ozelius et al., 2006). LRRK2 is a 290-kD polypeptide with multiple protein–protein interaction domains, including N-terminal armadillo, ankyrin, and LRR domains and C-terminal WD40 repeats, that flank enzymatically active Roc GTPase (Ras of complex proteins), COR, and kinase domains (Fig. 1 a). Several point mutations in the catalytic core of LRRK2 cause autosomal-dominant PD with incomplete penetrance (referred to herein as LRRK2-PD), while other mutations in the protein increase risk for sporadic PD (de Lau and Breteler, 2006; Kumari and Tan, 2009). The most common LRRK2-PD mutation, LRRK2 G2019S, falls in the kinase domain, as does the I2020T mutation. Several other PD-driving mutations, including R1441G/C/H and Y1699C, are located in the Roc and COR domains and promote GTP binding (Liao et al., 2014; Wu et al., 2019). A distinct set of LRRK2 mutations augments risk for Crohn's disease, leprosy, and tuberculosis (Hartlova et al., 2018; Liu et al., 2011; Liu and Lenardo, 2012; Zhang et al., 2009). How LRRK2 mutations cause PD is not well understood; however, mounting evidence supports a toxic gain-of-function mechanism with PD-driving LRRK2 mutations demonstrating abnormally augmented kinase activity (Steger et al., 2016; Taylor and Alessi, 2020). Certain PD mutants have also been shown to change LRRK2's affinity for binding partners (such as R1441 mutants, which do not bind 14-3-3 proteins), and others have been suggested to increase LRRK2 protein levels (Nichols et al.,

[1]Departments of Pathology, University of California San Francisco, San Francisco, CA; [2]Departments of Cellular and Molecular Pharmacology, University of California San Francisco, San Francisco, CA; [3]Departments of Cell and Tissue Biology, University of California San Francisco, San Francisco, CA; [4]Departments of Neurology, University of California San Francisco, San Francisco, CA; [5]Departments of Physiology, University of California San Francisco, San Francisco, CA; [6]Quantitative Biosciences Institute, University of California San Francisco, San Francisco, CA; [7]Taube/Koret Center for Neurodegenerative Disease Research, J. David Gladstone Institutes, San Francisco, CA; [8]Center for Systems and Therapeutics, J. David Gladstone Institutes, San Francisco, CA; [9]Department of Cell Biology, Erasmus MC, Rotterdam, The Netherlands; [10]Neuroscience, Merck & Co. Inc., Boston, MA; [11]Department of Biomedical Sciences, University of Sassari, Sassari, Italy; [12]Departments of Neurology and Neurotherapeutics, University of Texas Southwestern Medical Center, Dallas, TX; [13]Neuroscience, University of Texas Southwestern Medical Center, Dallas, TX; [14]Peter O'Donnell Jr. Brain Institute, University of Texas Southwestern Medical Center, Dallas, TX; [15]Department of Pathology, Stanford University, Palo Alto, CA; [16]Department of Oral and Craniofacial Sciences, School of Medicine, University of Missouri Kansas City, Kansas City, MO; [17]School of Dentistry and Department of Pediatrics, School of Medicine, University of Missouri Kansas City, Kansas City, MO; [18]Department of Pathology, University of Chicago, Chicago, IL; [19]Department of Pathology, University of California San Diego, San Diego, CA.

*M. FitzGibbon, E.M. Earley, and H. Ahrendt contributed equally to this paper. Correspondence to Annie Hiniker: ahiniker@ucsd.edu; Scott A. Oakes: soakes@bsd.uchicago.edu.

2010; Skibinski et al., 2014; Steger et al., 2016). LRRK2 kinase inhibition is being pursued as a possible therapeutic avenue for PD, with highly selective kinase inhibitors in clinical trials for LRRK2-driven and sporadic PD. An alternative approach that has not been explored is to reduce LRRK2 activity by exploiting cellular pathways that augment LRRK2 degradation, thus decreasing total LRRK2 protein levels.

The specific pathways regulating LRRK2 protein degradation are only beginning to be comprehensively evaluated, and both the autophagic-lysosome and ubiquitin-proteasome systems appear to be involved. LRRK2 has a complex relationship with autophagy: multiple studies implicate LRRK2 in regulating autophagy (Alegre-Abarrategui et al., 2009; Plowey et al., 2008), and a portion of LRRK2 appears to be degraded by chaperone-mediated autophagy (Orenstein et al., 2013). Additionally, a large fraction of endogenous LRRK2 has been shown to be degraded via the ubiquitin-proteasome system (Lobbestael et al., 2016); however, thus far, only two proteins are reported to act as E3 ubiquitin ligases for LRRK2: (1) WD repeat and SOCS box–containing 1 (WSB1), which ubiquitinates LRRK2 via atypical K27 and K29 linkages and causes LRRK2 aggregation but does not appear to promote proteasomal degradation (Nucifora et al., 2016); and (2) C-terminus of Hsc70-interacting protein (CHIP), an HSP70 cochaperone that interacts with many partially folded proteins (Ding and Goldberg, 2009; Ko et al., 2009). In keeping with its preference for misfolded proteins (Edkins, 2015), CHIP appears to be particularly important for turnover of destabilized LRRK2 variants, such as the sporadic PD modest-risk allele LRRK2 G2385R, and may not be as critical for other LRRK2-PD mutants (Rudenko et al., 2017).

LRRK2 is present at low levels in most cell types, hindering definitive determination of its endogenous subcellular localization. Predominantly through the use of overexpression systems, LRRK2 has been found to be (1) associated with endolysosomal and Golgi membranes, where it interacts with Rab GTPases (Purlyte et al., 2018); (2) present in the cytoplasm, where it binds the 14-3-3 family of adapter proteins (Rudenko and Cookson, 2010); and (3) present at the cytoskeleton, where it interacts with microtubules (Caesar et al., 2013; Kett et al., 2012). Strong evidence demonstrates that LRRK2 associates with membranes; important work identified 14 membrane-associated Rab proteins as kinase substrates of LRRK2, including Rab10 and Rab29 (Steger et al., 2017). Rab29, which localizes to Golgi network membranes, was also shown to be a unique activator of LRRK2's kinase activity, at least in cellular overexpression systems, as measured by LRRK2 autophosphorylation at Ser1292 and phosphorylation of substrate Rabs (Kalogeropulou et al., 2020 *Preprint*; Purlyte et al., 2018). Rab29 appears to preferentially activate Roc-COR domain LRRK2-PD mutants such as LRRK2 R1441G (Purlyte et al., 2018). The armadillo domain and conserved Leu-rich motifs in the ankyrin domain of LRRK2 have been shown to be important for LRRK2 to bind Rab29 (McGrath et al., 2019; Myasnikov et al., 2021; Purlyte et al., 2018).

LRRK2 localizes to the cytoplasm, where it associates with 14-3-3 proteins, a family of seven highly homologous isoforms that function as adaptor proteins to regulate myriad signaling pathways (Cau et al., 2018). The structural features mediating LRRK2's interaction with 14-3-3 have been rigorously investigated, and phosphorylation of LRRK2 serine residues Ser910 and Ser935 is required (Muda et al., 2014). LRRK2-PD mutants with decreased phosphorylation of Ser910 and Ser935 (predominantly species with mutations in the Roc-COR domain) show reduced affinity for 14-3-3 proteins (Li et al., 2011; Muda et al., 2014; Nichols et al., 2010). LRRK2's interaction with 14-3-3 appears necessary to maintain LRRK2 in the cytoplasm and may be one mechanism that prevents Rab29-mediated LRRK2 kinase activation. In support of this model, abnormal LRRK2 function has been implicated in idiopathic PD (i.e., PD negative for LRRK2 mutations): sensitive proximity ligation assays were used to demonstrate both increased kinase activity and decreased 14-3-3 binding of LRRK2 in substantia nigra neurons from patients with idiopathic PD compared with controls, strengthening the link between abnormalities in LRRK2 function and idiopathic PD (Di Maio et al., 2018).

A growing body of evidence indicates that LRRK2 can associate with the microtubule cytoskeleton. Multiple groups have demonstrated that overexpressed LRRK2 forms filamentous structures along microtubules (Caesar et al., 2013; Kett et al., 2012; Schmidt et al., 2019), which increase in frequency with kinase inhibitor treatment or point mutations in either the Roc-COR or kinase domains (Caesar et al., 2013; Kett et al., 2012; Schmidt et al., 2019). The in situ cryo-electron tomography structure of a truncated variant of PD-mutant LRRK2 I2020T bound to microtubules was solved to 14 Å, showing the Roc-COR domain adjacent to the microtubule and the kinase domain exposed to the cytoplasm (Watanabe et al., 2020). In keeping with this structure, LRRK2 can directly interact with β-tubulin through its Roc domain, altering tubulin acetylation and inhibiting axonal transport in neurons (Gandhi et al., 2008; Godena et al., 2014; Law et al., 2014). Recent work, which solved the structure of LRRK2 to 3.5 Å using cryo-EM, suggests that LRRK2's interaction with microtubules is regulated by the conformation of its kinase domain, and further, that LRRK2 binding to microtubules can disrupt axonal transport (Deniston et al., 2020). Axonal transport is restored by increasing microtubule acetylation, suggesting that the LRRK2–microtubule interaction is regulated and occurs only at specific subtypes of microtubules (Godena et al., 2014). However, additional upstream signals or binding partners regulating LRRK2 localization to microtubules have not previously been identified.

Here, we used a mass spectrometry (MS) interactome approach to find new LRRK2 binding partners and discovered the little-studied, microtubule-localized E3 ubiquitin ligase TRIM1. Whereas 14-3-3 stabilizes LRRK2 in the cytoplasm and Rab29 augments LRRK2's kinase activity at membranes, TRIM1 recruits LRRK2 to the microtubule cytoskeleton, where it mediates LRRK2 ubiquitination and proteasomal degradation. We narrowed down the TRIM1 binding site to nine amino acids (911–919) within a flexible interdomain ("regulatory loop" [RL]) region of LRRK2, $LRRK2_{853–981}$. LRRK2 RL contains Ser910 and Ser935, and the phosphorylation status of these serine residues influences LRRK2's choice of binding partner (14-3-3 versus

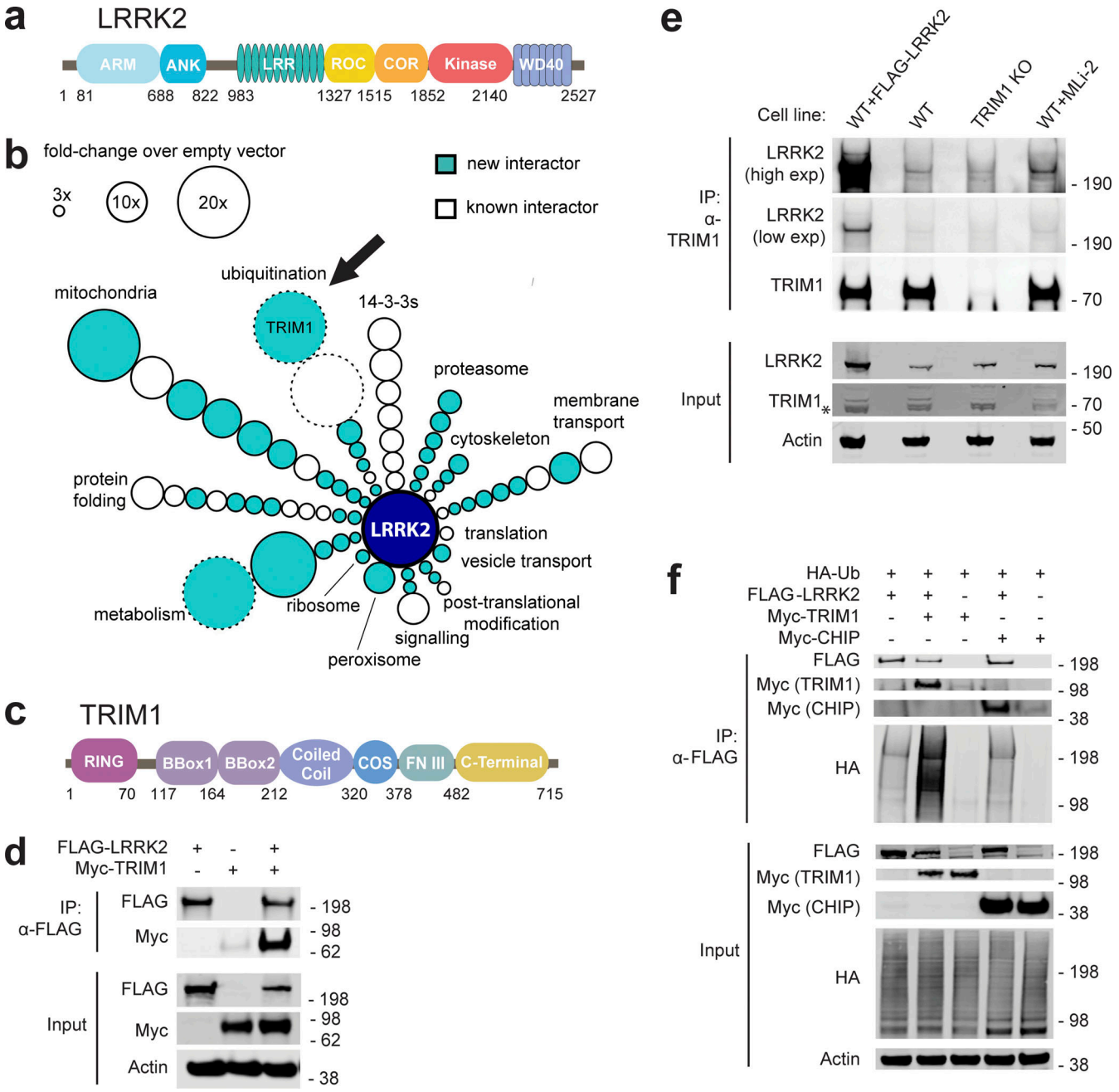

Figure 1. **TRIM1 is a new LRRK2 E3 ubiquitin ligase. (a)** Diagram of LRRK2 protein domains (ARM, armadillo repeat; ANK, ankyrin repeat; LRR, leucine-rich repeat; ROC, ras of complex proteins; COR, C-terminal of ROC domain). **(b)** Schematic of LRRK2 interactome in HEK-293T cells. LRRK2 interacting partners are classified radially according to function (aqua, new LRRK2 interacting partners; white, previously identified LRRK2 partners; size of circle indicates fold-change over empty vector control; circles without solid black outline had no peptides present in empty vector control; arrow indicates TRIM1). FLAG-LRRK2 was immunoprecipitated and interacting partners were identified and quantified by MS. Data represent at least four total independent replicates from two experiments and are additionally shown in Table S1. **(c)** Diagram of TRIM1 protein domains (FNIII, fibronectin III domain). **(d)** Coimmunoprecipitation of myc-TRIM1 with FLAG-LRRK2 in HEK-293T cells. **(e)** Coimmunoprecipitation of endogenous LRRK2 with TRIM1 in WT HEK-293T and HEK-293T TRIM1 CRISPR KO line. From left to right: WT HEK-293T cells transfected with exogenous FLAG-LRRK2 (positive control), WT HEK-293T cells, TRIM1 KO HEK-293T cells, and WT HEK-293T cells treated with 500 nM MLi-2 for 5 h. Low exp, short exposure of membrane; high exp, longer exposure of membrane. **(f)** Coimmunoprecipitation and ubiquitination of FLAG-LRRK2 with myc-TRIM1 or myc-CHIP in the presence of HA-ubiquitin in HEK-293T cells. Source data are available for this figure: SourceData F1.

TRIM1). Finally, TRIM1 inhibits Rab29-mediated activation of LRRK2 kinase activity and rescues PD-mutant LRRK2-driven toxicity, as measured by neurite outgrowth. Our studies show that TRIM1 is an important E3 ligase influencing LRRK2 subcellular location, protein levels, and function. They also suggest that LRRK2's RL is a critical structural element whose posttranslational modification is important in controlling LRRK2's binding to interacting partners, which in turn

regulates LRRK2 localization, turnover, kinase function, and toxicity.

Results

TRIM1 is a novel LRRK2 E3 ubiquitin ligase

We postulated that critical LRRK2 partners may have been missed in previous interaction studies, some of which used only a portion of the protein as bait (Beilina et al., 2014; Gandhi et al., 2008; Law et al., 2014; Salasova et al., 2017). We used an established affinity purification–MS approach, which has been extensively validated in our laboratory, to systematically and quantitatively identify the interactome of full-length LRRK2 (Jager et al., 2011). N-terminally FLAG-tagged full-length LRRK2 or FLAG-alone control plasmids were transiently transfected into HEK-293T cells (selected for our extensive library of baseline interactome data, allowing better exclusion of nonspecific interactors); lysates were affinity purified, and the eluted material was subjected to MS as in Jager et al. (2011). Interacting partners were determined by label-free MS1 quantification using MSStats (Choi et al., 2014). High-confidence interaction partners were proteins with an intensity more than threefold increased over empty vector control ($P < 0.05$), which identified >20 previously reported LRRK2-interacting proteins, including all members of the 14-3-3 family of proteins, as well as 48 novel partners, which were categorized according to function (Fig. 1 b and Table S1). The top hit was the putative E3 ubiquitin ligase, tripartite motif family 1 (TRIM1, also called MID2), which has never been described as playing a role in LRRK2 biology, although a prior proteomics study did identify TRIM1 as a possible LRRK2 interacting partner in HEK-293T cells (Salasova et al., 2017).

TRIM1 is a little-studied 78-kD protein whose coding sequence is located on the X-chromosome within the PARK12 genomic locus (Pankratz et al., 2003). It is a member of a ∼75-protein superfamily of E3 ubiquitin ligases with a common tripartite motif consisting of a RING domain, one or two B-box-type zinc fingers, and a coiled-coil domain (Meroni, 2012). TRIM1's tripartite motif is followed by a microtubule-targeting COS domain, a fibronectin type III domain, and a C-terminal domain (Fig. 1 c; Short and Cox, 2006). Although its cellular functions remain largely uncharacterized, TRIM1 missense mutations were reported in families with a rare form of X-linked mental retardation, indicating a critical role in normal brain function (Geetha et al., 2014). Consistent with our MS findings, myc-TRIM1 and FLAG-LRRK2 overexpressed in HEK-293T cells robustly coimmunoprecipitated (Fig. 1 d).

To validate the endogenous interaction of LRRK2 with TRIM1, we generated a TRIM1 knockout (KO) HEK-293T cell line using CRISPR/Cas9 gene editing. Genomic sequencing of the TRIM1 KO line identified two N-terminal frameshift mutations in the TRIM1 gene, leading to stop codons at amino acids 14 and 18 and no WT alleles of TRIM1. Because TRIM1 is expressed at low levels endogenously, it is not visible on immunoblot of HEK-293T cell lysates (Fig. 1 e, asterisk [*] in TRIM1 immunoblot of lysate indicates a nonspecific band). However, endogenous TRIM1 is detectable upon immunoprecipitation from HEK-293T cells. Immunoprecipitation of endogenous TRIM1 protein showed absence of TRIM1 protein in the TRIM1 KO line in contrast to the WT line. Overexpressed FLAG-LRRK2 robustly coimmunoprecipitated with endogenous TRIM1 (Fig. 1 e, lane 1). Endogenous LRRK2 coimmunoprecipitated with endogenous TRIM1 in the TRIM1 WT line, in contrast to the TRIM1 KO line (Fig. 1 e, compare lanes 2 and 3). We noted that this interaction was enhanced by addition of the LRRK2 kinase inhibitor MLi-2 for 5 h before immunoprecipitation (Fig. 1 e, compare lanes 2 and 4). Our data demonstrate that TRIM1 and LRRK2 interact under both overexpression and endogenous conditions.

Given that many TRIM family members are RING-finger E3 ubiquitin ligases, we speculated that TRIM1 may function to ubiquitinate LRRK2. We used an established in vivo ubiquitination assay for LRRK2, which was previously used to demonstrate LRRK2 ubiquitination by CHIP (the E3 ubiquitin ligase known to target LRRK2 for proteasomal degradation; Ko et al., 2009). We found that coexpression of myc-TRIM1 with FLAG-LRRK2 and HA-ubiquitin resulted in robust LRRK2 ubiquitination, with myc-CHIP serving as a positive control and HA-ubiquitin alone serving as a negative control (Fig. 1 f). Thus, TRIM1 is a novel E3 ubiquitin ligase for LRRK2.

TRIM1 recruits LRRK2 to microtubules

TRIM1 is part of the six-member C-I subfamily of TRIM proteins, all of which strongly associate with microtubules through a C-terminal COS domain (Short and Cox, 2006). Therefore, we hypothesized that LRRK2 may interact with TRIM1 at the microtubule cytoskeleton. Using overexpression studies, multiple groups have identified a portion of LRRK2 at microtubules (Caesar et al., 2013; Law et al., 2014); however, the fraction of LRRK2 associated with microtubules is generally very low in the absence of LRRK2 point mutations or kinase inhibitors (Godena et al., 2014; Kett et al., 2012). We used live-cell confocal microscopy to examine the subcellular distribution of transfected full-length GFP-LRRK2 in human lung H1299 cells, chosen for their large size and flat shape, allowing clear evaluation of the microtubule network. In agreement with previous studies, the vast majority of GFP-LRRK2 was cytoplasmic and did not colocalize with microtubules labeled with mCherry-tubulin (Fig. 2 a). We confirmed previous work demonstrating that mCherry-TRIM1 localizes to microtubules (Fig. 2 b; Buchner et al., 1999; Perry et al., 1999; Short and Cox, 2006). Strikingly, coexpression of mCherry-TRIM1 substantially increased GFP-LRRK2 colocalization with microtubules (Fig. 2 b and Video 1). We observed that mCherry-TRIM1 recruited GFP-LRRK2 to microtubules in all cell lines examined, including human lung carcinoma (A549) cells (Fig. S1 a), human neuroblastoma (SK-N-SH) cells (Fig. S1 b), and human embryonic kidney (HEK-293T) cells (Fig. S1 c), as well as human breast carcinoma (MCF7), and human (SH-SY5Y) and mouse (N2a) neuroblastoma cells (not depicted). Microtubule-localized GFP-LRRK2 showed a discontinuous appearance, in keeping with observations from other groups (Kett et al., 2012). Quantification of the percentage of cells with microtubule-associated GFP-LRRK2 in the presence of mCherry-TRIM1 versus mCherry-tubulin (Fig. 2 f) revealed that TRIM1 caused LRRK2 microtubule localization in essentially all cells in

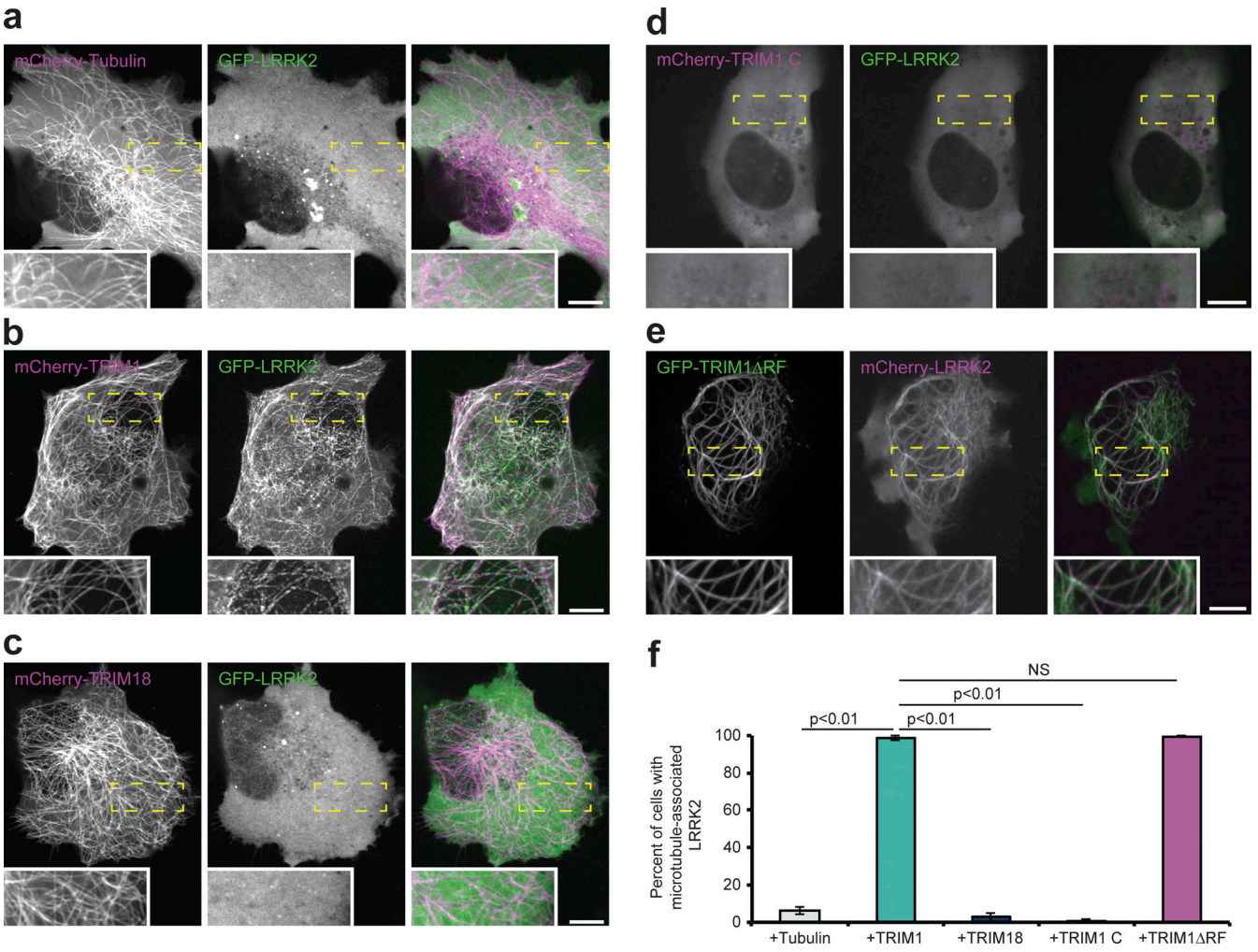

Figure 2. **TRIM1 coexpression recruits LRRK2 to microtubules.** Live-cell confocal microscopy of fluorescently tagged LRRK2 and tubulin, TRIM1, or TRIM18 constructs transiently transfected into H1299 cells. Insets in a–e show higher magnification of region identified by the yellow box. **(a)** In the presence of mCherry-tubulin, GFP-LRRK2 is diffusely cytoplasmic. From left to right: mCherry-tubulin, GFP-LRRK2, and merged image. **(b)** In the presence of mCherry-TRIM1, GFP-LRRK2 localizes to microtubules. From left to right: mCherry-TRIM1, GFP-LRRK2, and merged image. **(c)** In the presence of mCherry-TRIM18, GFP-LRRK2 is diffusely cytoplasmic. From left to right: mCherry-TRIM18, GFP-LRRK2, and merged image. **(d)** mCherry-TRIM1 C is cytoplasmic. When coexpressed with GFP-LRRK2, both remain diffusely cytoplasmic. From left to right: mCherry-TRIM1 C, GFP-LRRK2, and merged image. **(e)** GFP-TRIM1 ΔRF maintains microtubule localization and colocalizes with mCherry-LRRK2. From left to right: GFP-TRIM1 ΔRF, mCherry-LRRK2, and merged image. **(f)** Quantification of cells with microtubule-associated LRRK2 when coexpressed with indicated proteins in H1299 cells. 100 cells were evaluated in each condition in each of three independent experiments; bars show mean ± SD. Significance testing for f was performed using Kruskal–Wallis with post hoc Dunn test and Bonferroni correction. Scale bars = 10 µm.

which both proteins were expressed (98.7% ± 1.1%, mean ± SD), while only rare cells expressing mCherry-tubulin had visible LRRK2 at microtubules (6.3% ± 2.1%).

We next evaluated the specificity of the TRIM1-LRRK2 interaction in controlling LRRK2 microtubule localization. Of the ∼75 members of the TRIM family, TRIM1 is most homologous to TRIM18 (76% identical, 88% similar; Fig. S1 d). Like TRIM1, TRIM18 binds microtubules. Loss-of-function mutations in TRIM18 cause a syndrome of congenital midline defects (X-linked Opitz G/BBB syndrome), which has not been observed for TRIM1 mutations (Buchner et al., 1999). Coexpression of mCherry-TRIM18 was insufficient to recruit LRRK2 to microtubules (Fig. 2 c). The percentage of cells with GFP-LRRK2 at microtubules in the presence of mCherry-TRIM18 was 2.8% ± 2.5% (Fig. 2 f), which is statistically indistinguishable from that of mCherry-tubulin. Additionally, myc-TRIM18 did not robustly coimmunoprecipitate with FLAG-LRRK2 and its ability to ubiquitinate FLAG-LRRK2 was much diminished compared with myc-TRIM1 (Fig. 3 a). We also tested the ability of GFP-LRRK2 to bind TRIM9, which has the same domain organization as TRIM1 and TRIM18 (25% identical and 39% similar) and has been linked to PD in one study (Tanji et al., 2010). As with TRIM18, myc-TRIM9 failed to appreciably coimmunoprecipitate with LRRK2 (Fig. S1 e). Thus, the LRRK2-TRIM1 interaction appears highly specific.

To evaluate the extent to which TRIM1's microtubule-binding function is required for its E3 ligase activity, we constructed two variants of TRIM1, one which does not localize to microtubules

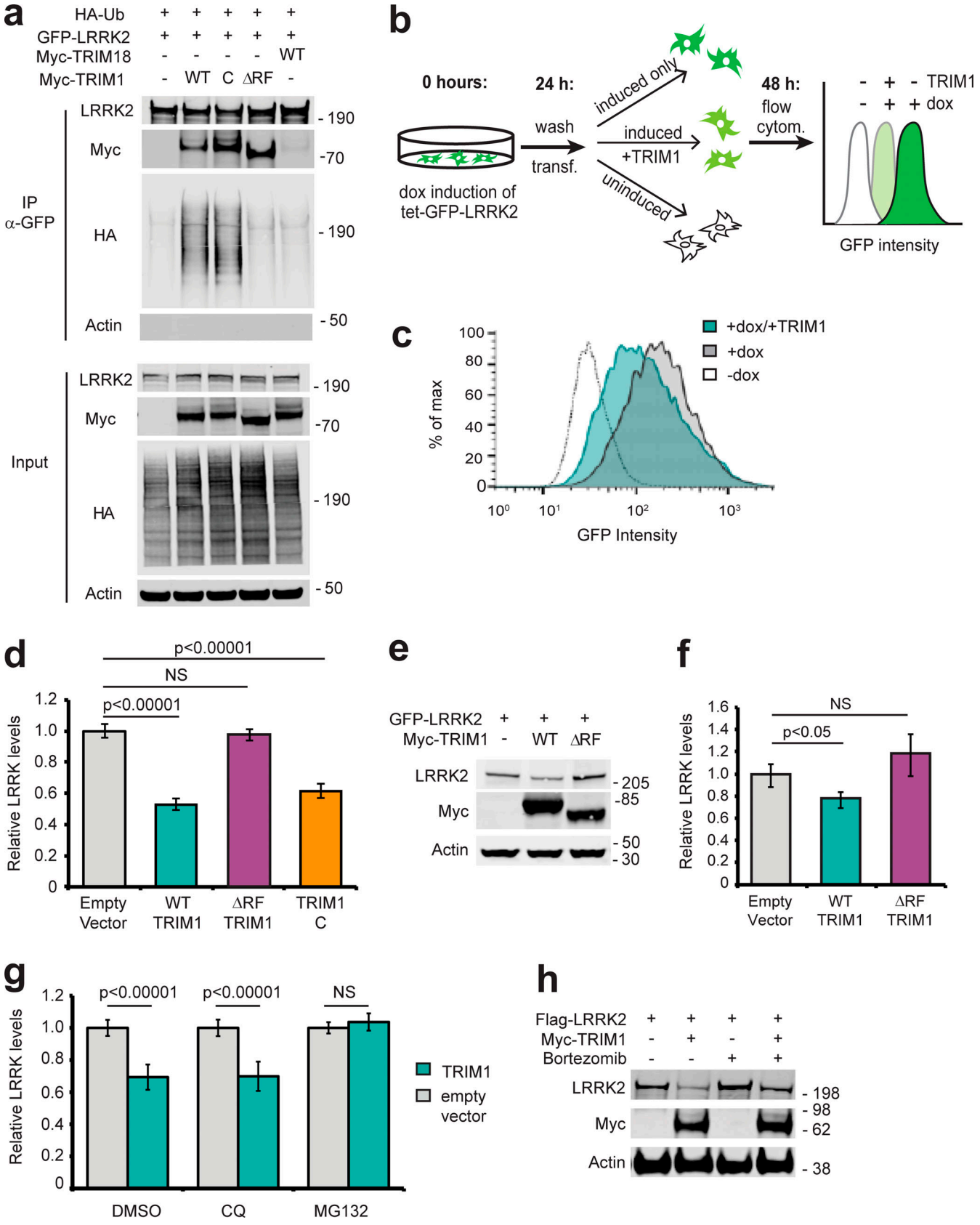

Figure 3. **TRIM1 ubiquitinates LRRK2 to regulate its proteasomal degradation. (a)** Immunoprecipitation and ubiquitination of GFP-LRRK2 with myc-TRIM1, myc-TRIM1 C, myc-TRIM1 ΔRF, or myc-TRIM18 in the presence of HA-ubiquitin (Ub) in HEK-293T cells. The immunoblotted membrane was physically cut between LRRK2- and myc-blotted portions, with both sections additionally probed with an anti-HA primary antibody. **(b)** Schematic of flow cytometric

assay using GFP fluorescence to measure GFP-LRRK2 turnover. Dox-inducible GFP-LRRK2 HEK-293T cells were induced for 18–24 h and transfected ("transf." in figure), dox was simultaneously withdrawn, and GFP fluorescence was measured after 18–24 h (additional validation of assay in Fig. S2). All flow cytometry ("flow cytom.") assays were performed in the dox-inducible GFP-LRRK2 HEK-293T cell lines described in Zhao et al. (2015). **(c)** Representative histograms of GFP-LRRK2 fluorescence in the absence or presence of dox followed by TRIM1 or empty vector transfection. **(d)** Quantification of GFP-LRRK2 levels 24 h after dox withdrawal in the presence of empty vector (gray bar), TRIM1 (green bar), TRIM1 ΔRF (purple bar), or TRIM1 C (orange bar). **(e)** Representative immunoblot of GFP-LRRK2 levels from dox-inducible HEK-293T cells in the presence of myc-TRIM1 WT, myc-TRIM1 ΔRF, or empty vector. **(f)** Quantification of panel e showing mean value with error bars (SEM). **(g)** Quantification of GFP-LRRK2 levels in the presence of chloroquine (CQ) at 25 µM for 24 h, MG132 at 2 µM for 24 h, or equivalent volume of DMSO vehicle. **(h)** Immunoblot of FLAG-LRRK2 levels with or without expression of myc-TRIM1 in the absence or presence of proteasomal inhibitor bortezomib (1 nM for 18 h) and in the presence of HA-ubiquitin. Bar graphs of flow cytometry assays (d and g) show normalized median green fluorescence intensity with error bars showing twice the SEM. All histograms and bar charts of flow cytometry results represent ≥10,000 single cells per condition. All coimmunoprecipitation and flow cytometry assay results show a representative experiment, with the experiment repeated a minimum of three times. Significance for flow cytometry data (d and g) was calculated using ANOVA with post hoc *t* test with Bonferroni correction. Significance testing for f was performed using Mann–Whitney *U* test. Source data are available for this figure: SourceData F3.

and is instead cytoplasmic, and the other which lacks the RING domain, eliminating its E3 ligase function. To construct the cytoplasmic variant of TRIM1, we used previous work on TRIM18 showing that mutating six amino acids in TRIM18's COS domain to alanine prevents TRIM18 from binding to microtubules and redirects it to the cytoplasm (Short and Cox, 2006). The identical amino acids are present in TRIM1 and were mutated to alanine (FLQ328AAA LDY377AAA; Fig. S1 d). The resulting construct, which we call TRIM1 C (for cytoplasmic), is diffusely cytoplasmic (Fig. 2 d) but retains E3 ligase activity and LRRK2 binding (Fig. 3 a). The RING finger deleted TRIM1 (TRIM1 ΔRF) is microtubule-bound (Fig. 2 e) but does not show E3 ligase activity (Fig. 3 a). The percentage of cells with GFP-LRRK2 at microtubules in the presence of mCherry-TRIM1 C was 0.7% ± 1.1%. The percentage of cells with mCherry-LRRK2 at microtubules in the presence of GFP-TRIM1 ΔRF was 99.7% ± 0.6% (Fig. 2 f). Therefore, TRIM1's ability to ubiquitinate LRRK2 can be separated from its ability to localize LRRK2 to the microtubule network.

Repeated attempts under multiple experimental conditions did not allow us to visualize the subcellular localization of endogenous LRRK2. Live-cell imaging was performed using A549 cells with an N-terminal GFP-tag added to *LRRK2* by CRISPR editing (gift of Dario Alessi, unpublished). Immunofluorescence using a variety of commercially available antibodies against LRRK2 (MJFF C41-2, UDD3, and N231) and GFP (13970; Abcam) was performed on the GFP-LRRK2 A549 line as well as WT versus CRISPR *LRRK2* KO A549 cells (gift of Dario Alessi), WT versus TALEN *LRRK2* KO murine RAW 264.7 macrophages (from the Michael J. Fox Foundation), and WT compared with siRNA *LRRK2* knockdown human melanoma Malme-3M cells. Under no experimental condition could we visualize a fluorescence signal specific to endogenous LRRK2. The inability to reproducibly visualize endogenous LRRK2 using these methods is in keeping with previous reports and highlights an important limitation in the field (Davies et al., 2013).

TRIM1 ubiquitinates LRRK2 to regulate its turnover via the proteasome

Polyubiquitin linkages frequently serve to target proteins for proteasomal or autophagic degradation, although they may also signal other molecular functions (Rajalingam and Dikic, 2016). Coexpression of TRIM1 with LRRK2 decreased LRRK2 accumulation over time compared with coexpression of control vector (Fig. S2 a, quantified in Fig. S2 b), suggesting that TRIM1-mediated ubiquitination of LRRK2 might target LRRK2 for degradation. To specifically measure changes in LRRK2 turnover in vivo, we created a doxycycline (dox)-inducible GFP-LRRK2 flow cytometric assay quantifying LRRK2 turnover. GFP-LRRK2 expression was induced to measurable but near physiologic levels (~10-fold higher than endogenous LRRK2 expression), dox was removed, and GFP fluorescence was measured by flow cytometry (a schematic of the experimental design is shown in Fig. 3 b). We first verified that normalized median GFP fluorescence intensity of GFP-LRRK2 was indeed proportional to LRRK2 levels on immunoblot (Fig. S2, c and d). We next tested the effect of TRIM1 expression on GFP-LRRK2 levels. As predicted, TRIM1 increased LRRK2 turnover—and thereby decreased LRRK2 levels (Fig. 3 c, quantified in Fig. 3 d). LRRK2 levels did not change in the presence of TRIM1ΔRF, demonstrating that TRIM1's effect was E3-ubiquitin ligase-dependent (Fig. 3 d). We validated that the changes measured by GFP-fluorescence were reflected on immunoblot (Fig. 3 e, quantified in Fig. 3 f). Consistent with our findings that TRIM1 C ubiquitinates LRRK2, LRRK2 levels were decreased by coexpression of TRIM1 C (Fig. 3 d). TRIM1 had no effect on turnover of dox-induced GFP alone (Fig. S2 e).

To define the pathway of TRIM1-catalyzed LRRK2 degradation, we measured TRIM1-mediated LRRK2 degradation in the presence of MG132 (proteasomal inhibitor) and chloroquine (autophagy inhibitor). LRRK2 degradation was inhibited by MG132, but not by chloroquine (Fig. 3 g), indicating that TRIM1-mediated degradation of LRRK2 occurs via the proteasome and not through autophagy. We validated by immunoblot that a second proteasomal inhibitor, bortezomib, restored TRIM1-mediated LRRK2 degradation (Fig. 3 h). Finally, we compared the effects of TRIM1 on LRRK2 levels to the effects of TRIM18 and CHIP in our dox-inducible GFP-LRRK2 line. Neither TRIM18 nor CHIP significantly decreased WT GFP-LRRK2 steady-state levels in this assay (Fig. S2 f). Thus, TRIM1 is a microtubule-localized E3 ligase that ubiquitinates LRRK2, causing its degradation via the proteasome.

We performed ubiquitin-specific MS on immunoprecipitated LRRK2 to identify TRIM1-mediated polyubiquitin chain types and ubiquitination sites. In HEK-293T cells, FLAG-myc-LRRK2 and either GFP-TRIM1 WT, GFP-TRIM1 ΔRF, or GFP was expressed in the presence and absence of MG132. From each of these six conditions, LRRK2 was sequentially immunoprecipitated with

anti-FLAG and anti-myc antibodies and then underwent ubiquitin-specific MS. K48 linkages (and no other ubiquitin linkage types) were identified in the LRRK2 sample containing WT GFP-TRIM1 and these K48 linkages were increased 3.5-fold in the presence of WT GFP-TRIM1 with MG132 (not depicted). No polyubiquitin linkages were identified in samples containing GFP-TRIM1 ΔRF or GFP, with or without MG132. No ubiquitination sites were identified on LRRK2 in any of these six samples, including after enrichment for ubiquitinated peptides before MS. We therefore repeated the experiment in the presence of HA-ubiquitin and used sequential FLAG and HA immunoprecipitation to more specifically isolate ubiquitinated LRRK2. In this experiment, 92 of 176 lysine residues in LRRK2 were identified (60% sequence coverage of LRRK2). A single site of ubiquitination, LRRK2 K831, was identified and found to be dependent on TRIM1's E3 ubiquitin ligase activity (Table S2 and Fig. S3 a). However, LRRK2 K831R was still ubiquitinated by TRIM1 (Fig. S3 b), suggesting that TRIM1 ubiquitinates additional sites on LRRK2.

In this more sensitive experiment, we identified K48, K63, and K11 polyubiquitin linkages at ≥10-fold abundance in the presence of WT TRIM1 compared with the presence of TRIM1 ΔRF or control vector (Fig. S3 c). Using antibodies specific for K48 and K63 linkages, we identified TRIM1-mediated K48 but not K63 linkages on LRRK2 in the presence of HA-ubiquitin, which were also catalyzed by TRIM1 C but were not catalyzed by TRIM1 ΔRF or TRIM18 (Fig. S3 d). To identify polyubiquitin chains directly conjugated to LRRK2 by TRIM1 in the absence of overexpressed ubiquitin, we used a pan-ubiquitin tandem ubiquitin binding entity (TUBE), which binds K6, K11, K48, and K63 polyubiquitin chains with nanomolar affinities. HEK-293T cells transfected with FLAG-LRRK2 and myc-TRIM1 or myc alone were treated with bortezomib and lysed in the presence of the deubiquitinase inhibitor PR-619. LRRK2 was immunoprecipitated with anti-FLAG antibodies and then eluted with FLAG peptide. From the LRRK2 elution, ubiquitinated LRRK2 was specifically isolated with a pan-selective TUBE (Fig. S3 e shows a schematic of the experiment). Lysates and eluates were immunoblotted with pan-ubiquitin, K48-specific, or K63-specific antibodies. TRIM1 increased the amount of total and K48-linked ubiquitin chains on LRRK2 but did not increase K63-linked chains (Fig. S3 f), demonstrating that TRIM1 mediates poly-K48 ubiquitination of LRRK2 to drive its proteasomal degradation. We were unable to identify a K11 chain–specific antibody or TUBE and so have not completely ruled out that K11-linked polyubiquitin may also mediate LRRK2 proteasomal degradation by TRIM1.

Knockdown of endogenous TRIM1 increases LRRK2 levels

To test the effect of endogenous TRIM1 on GFP-LRRK2 levels, we used a robust CRISPRi/dCas9 system (Larson et al., 2013) to knock down TRIM1 mRNA in conjunction with our flow cytometric GFP-LRRK2 assay. We generated dox-inducible GFP-LRRK2 cell lines stably expressing dCas9-BFP-KRAB. TRIM1 was knocked down using lentiviral transduction of sgRNA sequences targeted to the TRIM1 5′ UTR. TRIM1 sgRNA lowered TRIM1 mRNA levels to 20.0% ± 4.4% compared with control sgRNA (Fig. 4 a), with a resulting increase in GFP-LRRK2 protein levels of 38.3% ± 3.3% at 24 h (Fig. 4 b). This increase in GFP-LRRK2 protein levels was significant throughout the length of the experiment (≤44 h after dox withdrawal; Fig. S2 g), indicating a persistent LRRK2 turnover deficit in these cells. Thus, knockdown of endogenous TRIM1 decreases turnover of GFP-LRRK2, consistent with an important role for TRIM1 in LRRK2 degradation.

To examine the effects of TRIM1 on endogenous LRRK2 levels, we used human melanoma Malme-3M cells, which express relatively high levels of both LRRK2 and TRIM1 mRNA (NCBI GEO profiles IDs #86805339 and #86784306). siRNA against TRIM1 was used to knock down TRIM1 mRNA levels to 33% ± 6% relative to siRNA scrambled control (Fig. 4 c). TRIM1 knockdown resulted in an almost twofold increase (162% ± 13%) in endogenous LRRK2 levels at 48 h (Fig. 4, d and e). We also measured LRRK2 levels in TRIM1 CRISPR KO versus WT HEK-293T cells. In HEK-293T cells, the TRIM1 KO showed increased LRRK2 levels at steady state (136% ± 8% in TRIM1 KO versus 100% ± 7% in WT; Fig. 4, f and g). Thus, TRIM1 is a key regulator of endogenous LRRK2 turnover.

TRIM1 mediates LRRK2 turnover in neurons

We next tested TRIM1's ability to drive LRRK2 turnover in primary cortical neurons using optical pulse labeling, a method that has been used to monitor turnover of several neurodegenerative proteins, including huntingtin (Tsvetkov et al., 2013), α-synuclein (Skibinski et al., 2017), and TDP-43 (Barmada et al., 2014). In this assay, we quantified LRRK2 protein levels within individual neurons over multiple time points using the photoswitchable protein mEos3.2 fused to LRRK2. Cells expressing mEos3.2-LRRK2 initially fluoresce green; upon illumination with a 405-nm wavelength light, a population of green-mEos3.2-LRRK2 is irreversibly switched to red, creating a distinct pool of red-mEos3.2-LRRK2 in each neuron. Individual neurons were followed over time, and red-mEos3.2-LRRK2 signal was quantified using automated longitudinal imaging, allowing us to derive individual LRRK2 half-life measurements for each neuron (see schematic in Fig. 4 h). Embryonic day 20–21 rat primary cortical neurons were co-transfected with pGW1-GFP as a morphology marker, pGW1-mEos3.2-LRRK2 and either TRIM1 or a control plasmid, and photoswitched with a 5–8-s pulse of light at 405-nm wavelength. Neurons were imaged every 4–10 h for red and green fluorescence using custom-based automated algorithms to capture images in an unbiased and high-throughput manner. Representative neurons in the presence and absence of TRIM1 are shown in Fig. 4 i. In this neuronal system, as in the HEK-293T cell system, LRRK2 decay was significantly accelerated by almost twofold in the presence of TRIM1 ($t_{1/2}$ LRRK2 = 24.9 h in the absence of exogenous TRIM1; $t_{1/2}$ LRRK2 = 15.9 h in the presence of exogenous TRIM1, P = 0.025; 113 and 87 neurons per group respectively, three independent experiments).

The interdomain region between LRRK2's ankyrin and LRR domains binds TRIM1

To better define the TRIM1/LRRK2 interaction, we performed a series of coimmunoprecipitation (co-IP) experiments using

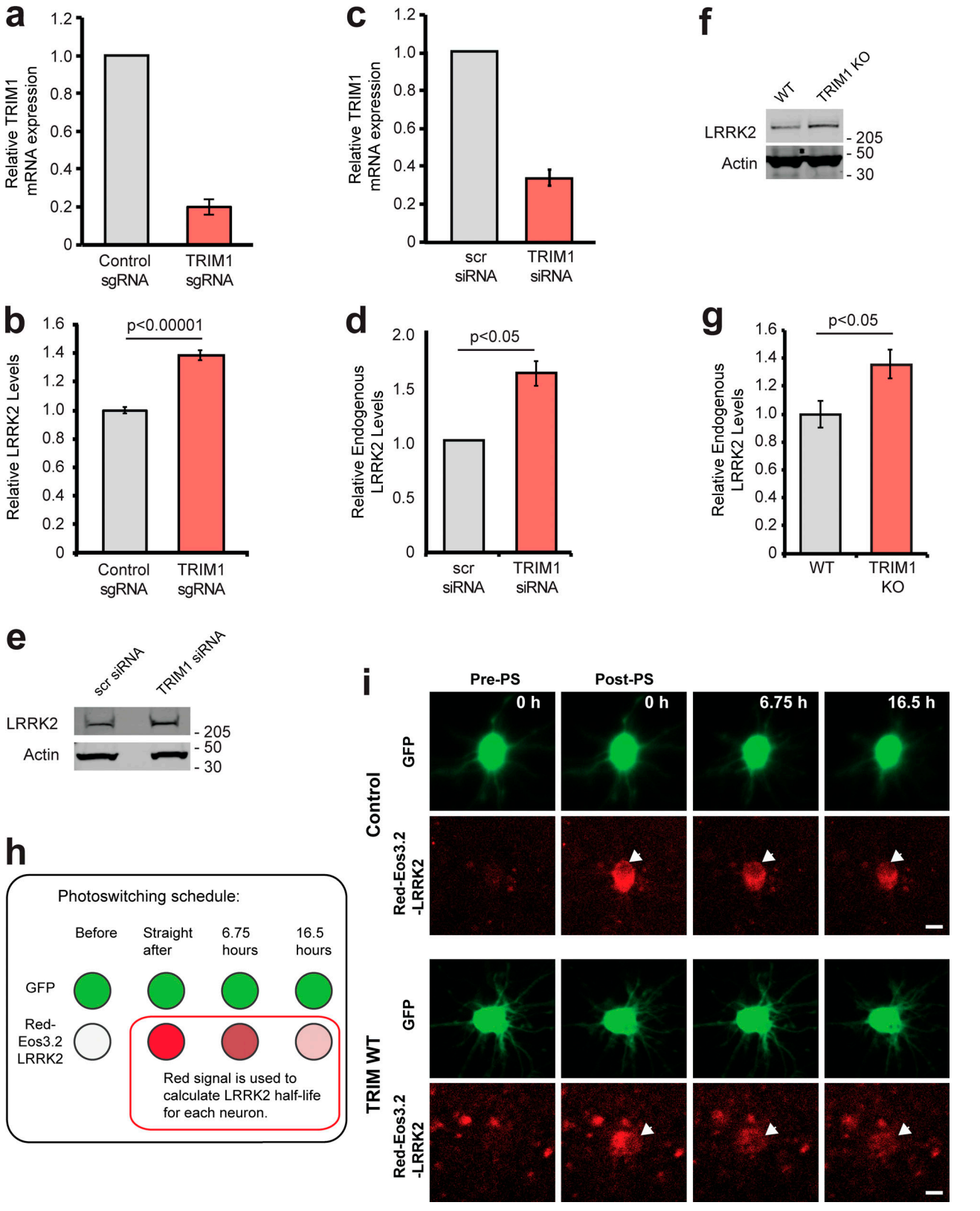

Figure 4. **Reducing endogenous TRIM1 levels increases LRRK2 levels. (a)** Relative TRIM1 mRNA expression in dox-inducible GFP-LRRK2 HEK-293T cells with dCas9 and either nontargeting sgRNA (gray bar) or four pooled TRIM1-targeting sgRNAs (red bar). Bars indicate mean ± SD. **(b)** Quantification of GFP-LRRK2 fluorescence with TRIM1 knocked down (red bar) compared with cells with nontargeting sgRNA (gray bar) 24 h after dox withdrawal. Error bars are twice the SEM; minimum of 10,000 live, single cells analyzed per condition. **(c)** Relative TRIM1 mRNA expression in Malme-3M cells with either scrambled siRNA (gray bar) or TRIM1-targeting siRNA (red bar) from the six independent experiments quantified in panel d. **(d)** Quantification of endogenous LRRK2 levels measured by immunoblots after TRIM1 siRNA knockdown showing mean values from six independent experiments; error bars show SEM. scr, scrambled.

(e) Representative immunoblot of endogenous LRRK2 in lysate of Malme-3M cells with scrambled siRNA (left lane) or endogenous TRIM1 knocked down by targeted siRNA (right lane). **(f)** Immunoblot of endogenous LRRK2 in WT and TRIM1 KO HEK-293T cells. **(g)** Quantification of panel f showing mean value from four independent experiments, with error bars showing SEM. **(h)** Schematic of optical pulse-labeling experiment in which primary cortical neurons were cotransfected with mEos3.2-LRRK2 and GFP, and either TRIM1 or control plasmid. Cells were pulsed for 5–8 s with 405-nm light, causing a portion of mEos3.2-LRRK2 to fluoresce red, and cells were imaged over the indicated time period. **(i)** Representative primary cortical neurons from photoswitching (PS) experiment. Before photoswitching (pre-PS), mEos3.2-Red-LRRK2 was not detected. After photoswitching (post-PS) mEos3.2-Red-LRRK2 was detected, nuclear excluded (arrow), and decayed with time. LRRK2 decayed faster in neurons transfected with TRIM1. Scale bar = 10 µM. P value for b calculated using *t* test. Significance testing for d and g calculated using Mann–Whitney *U* test. Source data are available for this figure: SourceData F4.

truncation mutants of both proteins (domain structure of LRRK2 truncation mutants illustrated in Fig. S4 a). We found that LRRK2 interacts with the tandem B-box domain of TRIM1 (Fig. 5 a), with binding most dependent on TRIM1's linker and B-box1 domain (Fig. 5 b). Notably, with the exception of the extreme C-terminus, this domain includes the portion of least homology to TRIM18 (Fig. S1 d, double red line), suggesting that variations in this region may account for the differential ability of these highly homologous TRIM family members to bind LRRK2.

LRRK2 constructs lacking the interdomain region between the ankyrin and LRR domains (amino acids 822–982) were markedly reduced in their ability to bind full-length TRIM1 (Fig. 5 c, asterisks [*] denote constructs with strongly decreased binding, and Fig. S4 a). A truncated $LRRK2_{822–982}$ mutant was sufficient for binding to TRIM1 (Fig. 5 c, far right lane). $LRRK2_{822–982}$ was also sufficient for TRIM1-mediated LRRK2 localization to microtubules (Figs. 5 d and S4 a). Interestingly, the interdomain region that binds TRIM1 is absent from LRRK2's closest homologue, LRRK1 (Sejwal et al., 2017). This region is already known to be critical in mediating binding of 14-3-3 proteins, LRRK2's best understood interactors (Nichols et al., 2010). It has also been shown to undergo significant phosphorylation in response to upstream kinases, suggesting it is a key LRRK2 regulatory region (Muda et al., 2014). In silico modeling of the secondary structure of $LRRK2_{822–982}$ predicts it to be >75% unstructured and >75% solvent exposed (https://predictprotein.org/). This is consistent with a recent cryo-EM structure of full-length LRRK2, which demonstrated a hinge helix (amino acids 834–852) followed by an unstructured region not amenable to cryo-EM (amino acids 853–981; Myasnikov et al., 2021). From here on, we designate $LRRK2_{853–981}$ the LRRK2 regulatory loop (LRRK2 RL) region (Fig. 5 e). Within LRRK2 RL, we performed alanine scanning to pinpoint the precise amino acids required for LRRK2's interaction with TRIM1. We identified a 9-amino acid region (amino acids 911–919) required for LRRK2 binding as measured by co-IP (Fig. 5 f). Consistently, these 9 amino acids were also required for TRIM1 to cause LRRK2 microtubule localization (Fig. 5 g) and for TRIM1 to ubiquitinate LRRK2 (Fig. 5 h).

LRRK2 RL phosphorylation influences TRIM1 versus 14-3-3 binding

Interaction of 14-3-3 with LRRK2 has been studied in detail (Cau et al., 2018). This interaction depends on the phosphorylation state of multiple LRRK2 serine residues, with Ser910 and Ser935 phosphorylation absolutely required for the LRRK2-14-3-3 interaction (Dzamko et al., 2010). Since Ser910 and Ser935 are located within LRRK2 RL, directly adjacent to the 9 amino acids required for TRIM1 binding, we postulated that TRIM1 and 14-3-3 might compete for LRRK2 binding. Specifically, we hypothesized that Ser910 and Ser935 phosphorylation influences LRRK2 RL's predilection for binding partners. To visualize the subcellular localization of LRRK2 in the presence of both 14-3-3 and TRIM1, we transfected H1299 cells with mCherry-LRRK2, EBFP2-14-3-3 θ, and GFP-TRIM1. In the absence of GFP-TRIM1, both mCherry-LRRK2 and EBFP2-14-3-3 showed a diffusely cytoplasmic localization (Fig. S4 b). In the presence of GFP-TRIM1, mCherry-LRRK2 associated with microtubules, while EBFP2-14-3-3 remained diffusely cytoplasmic (Figs. 6 a and S4 c). We quantified the proportion of cells with microtubule-associated mCherry-LRRK2 in the presence of EBFP2-14-3-3 and/or GFP-TRIM1 and found that TRIM1 caused LRRK2 localization to microtubules in essentially all cells in which both proteins were expressed, regardless of the presence of overexpressed 14-3-3 (94.2% ± 1.7% without 14-3-3; 92.0% ± 2.6% with 14-3-3; Fig. 6 b). No cells (0% ± 0%) showed mCherry-LRRK2 at microtubules in the presence of EBFP2-14-3-3 alone. Thus, GFP-TRIM1 causes mCherry-LRRK2 microtubule association in both the absence and presence of overexpressed EBFP2-14-3-3.

To characterize residues in LRRK2 that influence its binding to TRIM1 versus 14-3-3, we quantified co-IP of 14-3-3 with various LRRK2 point mutants in the presence and absence of TRIM1. GFP-LRRK2-WT and V5-14-3-3 θ coimmunoprecipitated in the absence of myc-TRIM1, as reported in the literature (Fig. 6 c; Manschwetus et al., 2020; Nichols et al., 2010). In the presence of both V5-14-3-3 and myc-TRIM1, GFP-LRRK2-WT robustly coimmunoprecipitated myc-TRIM1 but only bound 10% as much V5-14-3-3 as it did in the absence of myc-TRIM1 (Fig. 6 d), demonstrating that TRIM1 can disrupt LRRK2's binding to 14-3-3. To test whether Ser910 and Ser935 phosphorylation is required for LRRK2 binding to TRIM1, we mutated GFP-LRRK2 Ser910 and Ser935 to nonphosphorylatable alanines (GFP-LRRK2 SA). As demonstrated by others, GFP-LRRK2-SA did not bind V5-14-3-3 (Nichols et al., 2010). In contrast, myc-TRIM1 coimmunoprecipitated with GFP-LRRK2-SA to the same extent as with GFP-LRRK2-WT (Fig. 6 c). Lack of binding of GFP-LRRK2-SA to 14-3-3 did not change in the presence of myc-TRIM1 (Fig. 6 d). Thus, TRIM1 strongly binds both LRRK2 WT and nonphosphorylatable LRRK2-SA, while 14-3-3 selectively binds LRRK2 WT, in which S910 and S935 can be phosphorylated.

We also tested the LRRK2 PD mutant LRRK2 R1441C, which lacks S910 and S935 phosphorylation and does not bind 14-3-3. LRRK2 R1441C strongly bound myc-TRIM1 but did not coimmunoprecipitate with V5-14-3-3 (Fig. 6, c and d). Finally, we attempted to construct a phosphomimetic version of GFP-LRRK2

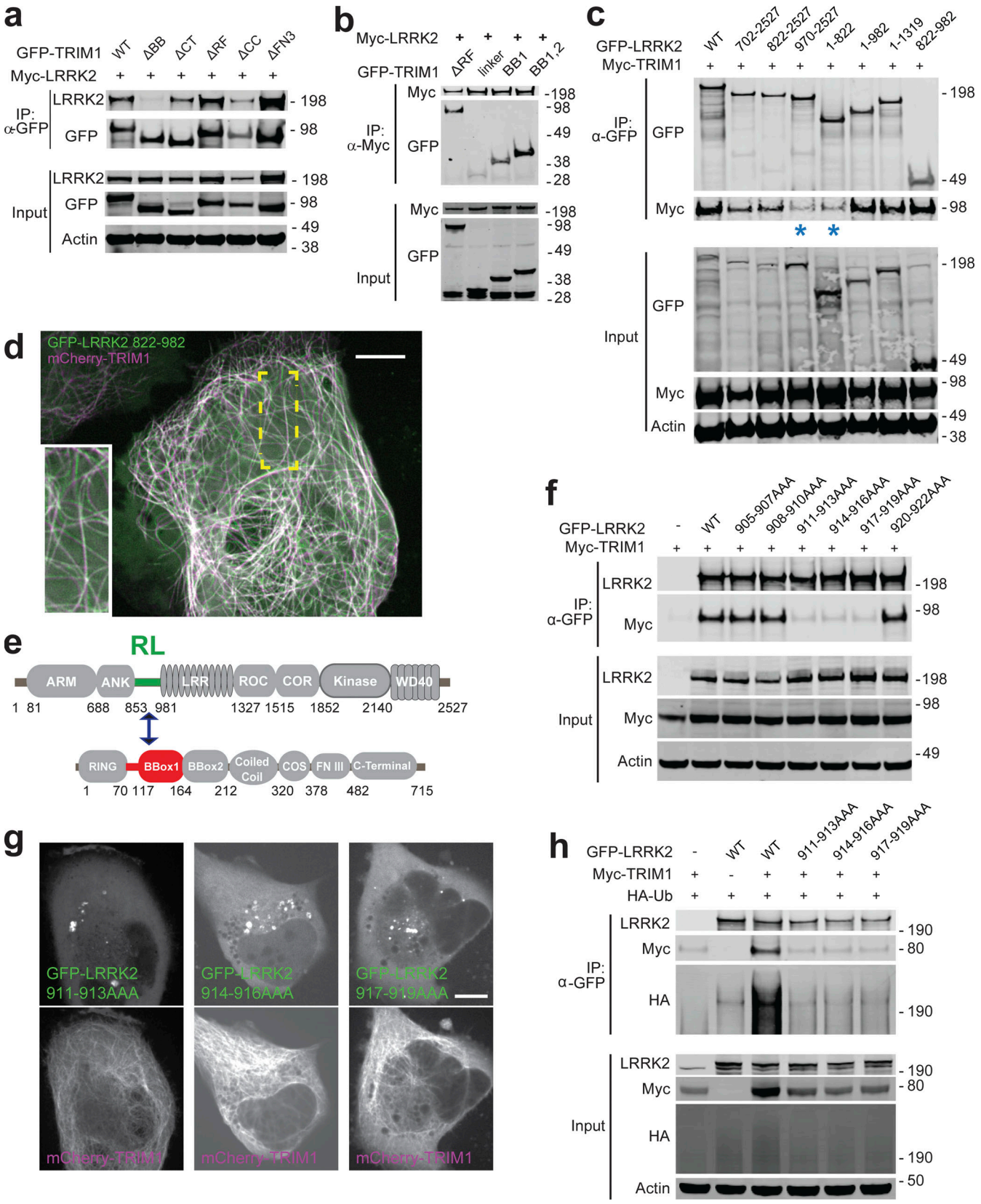

Figure 5. **TRIM1 binds an N-terminal LRRK2 regulatory loop region via its B-box domain. (a)** Coimmunoprecipitation of full-length myc-LRRK2 with GFP-TRIM1 domain constructs in HEK-293T cells (ΔBB, TRIM1 construct lacking both B-box domains; ΔCT, TRIM1 lacking C-terminal domain; ΔRF, TRIM1 lacking ring-finger domain; ΔCC, TRIM1 lacking coiled coil domain; ΔFN3, TRIM1 lacking fibronectin III domain; details of constructs in Short et al. (2002). **(b)** Coimmunoprecipitation of full-length myc-LRRK2 with GFP-TRIM1 B-box domain constructs in HEK-293T cells (ΔRF denotes $TRIM1_{70–715}$; linker denotes

TRIM1$_{70–117}$; BB1 denotes TRIM1$_{70–164}$; BB1,2 denotes TRIM1$_{70–212}$). **(c)** Coimmunoprecipitation of full-length myc-TRIM1 with GFP-LRRK2 domain constructs in HEK-293T cells. LRRK2 constructs include indicated amino acids from full-length LRRK2 sequence and are illustrated in Fig. S4. LRRK2$_{822–892}$ is sufficient for interaction with TRIM1. **(d)** Live-cell confocal microscopy of GFP-LRRK2$_{822–982}$ and mCherry-TRIM1 transiently transfected into H1299 cells. Inset shows higher magnification of region identified by the yellow box. Scale bar = 10 µM. **(e)** Schematic of LRRK2-TRIM1 domain interaction mediated by the LRRK2 Regulatory Loop (RL, green) and TRIM1$_{BBox1}$ (red). **(f)** Coimmunoprecipitation of full-length myc-TRIM1 with GFP-LRRK2 WT and RL alanine scanning mutants. Mutants are full-length LRRK2 constructs with the three amino acid residues indicated mutated to three alanines. **(g)** Live-cell confocal microscopy of GFP-LRRK2 RL alanine scanning mutants and mCherry-TRIM1 transiently transfected into H1299 cells. Scale bar = 10 µM. **(h)** Ubiquitination of immunoprecipitated GFP-LRRK2 WT versus RL alanine scanning mutants. All coimmunoprecipitation and microscopy experiments are a representative image of at least three independent experiments. Source data are available for this figure: SourceData F5.

by mutating Ser910 and Ser935 to aspartic acid (GFP-LRRK2 SD). TRIM1 bound GFP-LRRK2-SD to a similar extent as GFP-LRRK2-WT. However, GFP-LRRK2-SD did not bind 14-3-3 in the presence or absence of TRIM1, indicating that GFP-LRRK2-SD does not adequately mimic phosphorylated Ser910 and Ser935 (Fig. 6 c). Thus GFP-LRRK2-SD does not provide information regarding the extent to which phosphorylated LRRK2 binds TRIM1.

We next measured the phosphorylation state of LRRK2 bound to either TRIM1 or 14-3-3 using co-IP followed by quantitative immunoblot with phosphospecific antibodies against either phospho-Ser910 or phospho-Ser935 LRRK2. LRRK2 bound to 14-3-3 showed markedly increased phosphorylation of both Ser910 and Ser935 compared with LRRK2 bound to TRIM1 (Fig. 6 e, compare red [phospho] to green [total] signal of immunoprecipitated LRRK2). We quantified the ratio of phospho-LRRK2 to total LRRK2 signal for 14-3-3–bound LRRK2 and TRIM1-bound LRRK2 (normalized to phospho-LRRK2:total-LRRK2 in the input lysate; Fig. 6 f). Ser935 phosphorylation of TRIM1-bound LRRK2 was 27% of 14-3-3-bound LRRK2 (ratio of phospho-S935 LRRK2:total LRRK2 signal was 0.26 ± 0.13 for TRIM1-bound LRRK2 and 0.94 ± 0.13 for 14-3-3–bound LRRK2). Similarly, LRRK2 Ser910 phosphorylation of TRIM1-bound LRRK2 was 28% of 14-3-3-bound LRRK2 (ratio of phospho-S910 LRRK2: total LRRK2 was 0.21 ± 0.02 for TRIM1-bound LRRK2 and 0.74 ± 0.12 for 14-3-3–bound LRRK2). Thus, phosphorylation of LRRK2's RL region influences LRRK2's affinity for partner proteins, with a larger proportion of unphosphorylated LRRK2 bound to TRIM1 than to 14-3-3. Together, these data suggest that TRIM1 binds both nonphosphorylated and phosphorylated LRRK2 and localizes it to microtubules, whereas 14-3-3 preferentially binds phosphorylated LRRK2 in the cytosol.

Type 1 LRRK2 kinase inhibitors increase TRIM1-LRRK2 association

Type 1 LRRK2 kinase inhibitors such as MLi-2 increase LRRK2's microtubule localization and cause LRRK2 ubiquitination and proteasomal degradation through unknown mechanisms (Deniston et al., 2020; Zhao et al., 2015). Because TRIM1 expression phenocopies the effects of MLi-2 treatment (i.e., causes LRRK2 localization to microtubules and leads to LRRK2 ubiquitination and degradation), we hypothesized that TRIM1 may be required for LRRK2 degradation after type 1 inhibitor treatment. We first tested whether MLi-2 treatment increases colocalization of LRRK2 and TRIM1 at microtubules. H1299 cells transfected with GFP-LRRK2 and mCherry-TRIM1 were treated with MLi-2, and time-lapse live-cell microscopy was performed. We focused on the rare subset of cells with predominantly cytoplasmic GFP-LRRK2 in the presence of mCherry-TRIM1 before treatment with MLi-2. 30 min after treatment with 200 nM MLi-2, GFP-LRRK2 and mCherry-TRIM1 were strongly associated at microtubules (Figs. 6 g and S5 a), which continued for the duration of the experiment (120 min). GFP-LRRK2 association with TRIM1 and with the microtubule network did not increase after vehicle-alone treatment. To test the effect of MLi-2 on association of endogenous LRRK2 and TRIM1, we coimmunoprecipitated LRRK2 with TRIM1 in HEK-293T cells treated with MLi-2. Under endogenous conditions, we observed increased association of LRRK2 and TRIM1 in the presence of MLi-2 compared with the absence of MLi-2 (Fig. 1 e, lanes 2 and 4).

To test whether TRIM1 is required for LRRK2 degradation after type 1 kinase inhibitor treatment, we measured GFP-LRRK2 levels after MLi-2 or vehicle treatment using the dCas9/dox-GFP-LRRK2 system. MLi-2 treatment at 100 nM for 24 h decreased GFP-LRRK2 levels by ∼50%, consistent with what others have observed (Fig. S5 b, compare vehicle to MLi-2 treatment in the presence of control sgRNA; Lobbestael et al., 2016; Zhao et al., 2015). If TRIM1 is required for LRRK2 degradation after MLi-2 treatment, TRIM1 knockdown should rescue LRRK2 levels in the presence of MLi-2. We therefore measured the effect of TRIM1 knockdown on LRRK2 levels after MLi-2 treatment. As we had previously shown (see Figs. 4 b and S2 g), in the absence of MLi-2, TRIM1 knockdown increased LRRK2 levels compared with control sgRNA. In the presence of MLi-2, TRIM1 knockdown caused no additional rescue of LRRK2 levels compared with control sgRNA (Fig. S5 b; vehicle-treated LRRK2 levels are normalized to 1). In control cells, MLi-2 treatment led to a 52.2% ± 3% decrease in total LRRK2 levels compared with vehicle, and in cells with TRIM1 knocked down, MLi-2 caused a 54.8% ± 4.4% decrease in LRRK2 compared with vehicle. We thus conclude that while TRIM1 mediates basal LRRK2 turnover, TRIM1 is not required for LRRK2 degradation after MLi-2 treatment. Hence, the mechanisms responsible for kinase inhibitor–mediated LRRK2 turnover remain to be discovered.

TRIM1 inhibits LRRK2 kinase activation by Rab29

Rab29, which is found at Golgi network membranes, was identified as a strong activator of LRRK2 kinase function in cell-based overexpression systems (Kalogeropulou et al., 2020 *Preprint*; Purlyte et al., 2018). Rab29 overexpression increases LRRK2 autophosphorylation at Ser1292 and LRRK2 phosphorylation of substrate Rab proteins (Rab10 at Thr73 and Rab29 at Thr71; these phosphorylation sites are LRRK2 specific; Purlyte et al., 2018). The N-terminal portion of LRRK2 interacts with

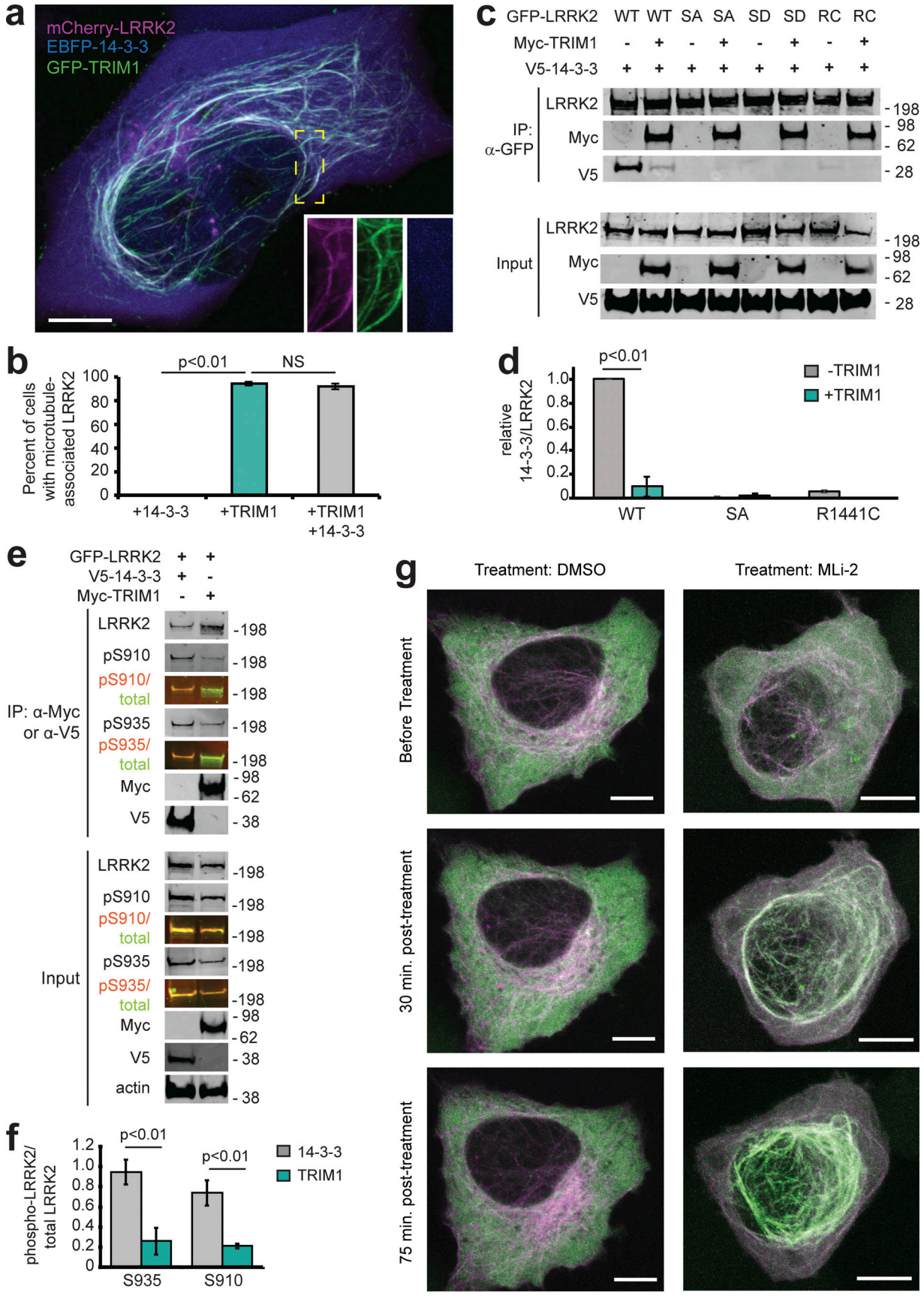

Figure 6. **TRIM1 competes with 14-3-3 to bind LRRK2's regulatory loop and recruit LRRK2 to microtubules. (a)** Live-cell confocal microscopy of mCherry-LRRK2 in the presence of EBFP2-14-3-3 and GFP-TRIM1. Scale bar = 10 µM. **(b)** Quantification of H1299 cells with microtubule-associated LRRK2

when coexpressed with indicated proteins. 100 cells were evaluated in each experiment; bars indicate mean ± SD (two independent experiments). **(c)** Coimmunoprecipitation of GFP-LRRK2 WT, Ser910Ala Ser935Ala (SA), Ser910Asp Ser935Asp (SD), or R1441C (RC) with V5-14-3-3 theta in the presence and absence of myc-TRIM1 in HEK-293T cells. **(d)** Quantification of panel c showing mean values from three independent experiments, with error bars showing ± SD. Significance determined by Mann–Whitney *U* test. **(e)** Coimmunoprecipitation of GFP-LRRK2 with either V5-14-3-3 theta or myc-TRIM1 in HEK-293T cells. Overlaid immunoblots in color show relative ratio of phospho- to total-LRRK2 (total LRRK2 in green, antibody is NeuroMab clone N241A/34; phospho-LRRK2 is in red, antibodies are phospho-Ser910 [Abcam, UDD 1 15(3)] and phospho-Ser935 [UDD 2 10(12); Abcam]). **(f)** Quantification of e with mean ± SEM from three independent experiments. **(g)** Live-cell confocal microscopy of GFP-LRRK2 in the presence of mCherry-TRIM1 after treatment with LRRK2 kinase inhibitor MLi-2 (200 nM) or vehicle. Rare cells with low levels of colocalization before treatment were followed. LRRK2 is shown in green and TRIM1 in purple. Images from isolated channels are shown in Fig. S5 c. Scale bar = 10 µM. All live-cell images and coimmunoprecipitation experiments are a representative image of at least three independent experiments. Significance testing for panel b was performed using Kruskal–Wallis with post hoc Dunn test and Bonferroni correction and Mann–Whitney *U* test for d and f. Source data are available for this figure: SourceData F6.

Rab29. In particular, the C-terminal half of LRRK2's armadillo domain is critical for LRRK2–Rab29 interaction (McGrath et al., 2019). Conserved Leu-rich motifs in LRRK2's ankyrin domain—which is near LRRK2 RL—also appear essential for LRRK2 activation by Rab29 (Purlyte et al., 2018). We hypothesized that TRIM1 might inhibit the ability of Rab29 to activate LRRK2's kinase activity. To measure TRIM1's effect on Rab29-mediated LRRK2 activation, we dox-induced GFP-LRRK2 WT or R1441G expression in HEK-293T cells and coexpressed myc-TRIM1 and/or HA-Rab29 via transient transfection. In these experiments, we provided continuous high-level (1 µg/ml) dox induction until the time of harvest to maintain equivalent LRRK2 levels in the presence and absence of TRIM1 and used quantitative immunoblot to validate that total LRRK2 levels were equivalent in all conditions (not shown).

Consistent with others' work, overexpressed Rab29 increased LRRK2 WT and LRRK2 R1441G kinase activity approximately two- to fourfold, as measured by autophosphorylation of LRRK2 Ser1292 (Fig. 7 a, quantified in Fig. 7 b; Purlyte et al., 2018). Coexpression of TRIM1 in the setting of Rab29 overexpression decreased phosphorylation of LRRK2 Ser1292 to baseline levels (i.e., levels observed without Rab29 overexpression) for both LRRK2 WT and LRRK2 R1441G. TRIM1 coexpression had no effect on Ser1292 phosphorylation in the absence of Rab29 (Fig. 7, a and b). We quantified phosphorylation of Rab29 at Thr71 and Rab10 at Thr73 as additional measures of LRRK2 kinase activity. Coexpression of TRIM1 decreased phosphorylation of Rab29 Thr71 by about half for LRRK2 WT (44% ± 5%) and LRRK2 R1441G (58% ± 7%; Fig. 7 a, quantified in Fig. 7 c). Coexpression of TRIM1 modestly decreased phosphorylation of endogenous Rab10 Thr73 by LRRK2 WT (70% ± 9%) and LRRK2 R1441G (71% ± 8%) but did not fully restore to baseline levels without Rab29 (Fig. 7 a, quantified in Fig. 7 d). Coexpression of only TRIM1 with LRRK2 had no effect on Thr73 Rab10 phosphorylation, similar to our findings for LRRK2 Ser1292. Together, these data show that TRIM1 inhibits Rab29-mediated LRRK2 kinase activation but does not appear to have an effect on basal LRRK2 kinase activity.

To begin to dissect the mechanism by which TRIM1 inhibits Rab29-mediated LRRK2 kinase activation, we measured phosphorylation of Rab29 Thr71 in the presence of WT TRIM1, TRIM1 C (intact E3 ligase activity and cytoplasmic), TRIM1 ΔRF (no E3 ligase enzymatic activity but still binds microtubules), or control vector. We used phosphorylation of Rab29 Thr71 because it is our most robust readout of LRRK2 kinase activation: on quantitative immunoblot, phospho-Thr71 Rab29 signal is 20–100× higher than phospho-Ser1292 LRRK2 or phospho-Thr73 Rab10. Identically to WT TRIM1, TRIM1 C inhibited Rab29-mediated LRRK2 activation for both LRRK2 WT and R1441G (Fig. 8 a, quantified in Fig. 8 c, top panel). TRIM1 ΔRF did not inhibit Rab29-mediated LRRK2 activation, suggesting that TRIM1's E3 ubiquitin ligase domain is required for inhibition. Mutation of Lys831, the ubiquitinated LRRK2 residue identified by MS, to Arg (LRRK2 K831R) did not rescue TRIM1's inhibition of Rab29-mediated LRRK2 activation (Fig. S5 c, quantified in Fig. S5 d).

We further investigated the mechanism of TRIM1's inhibition of Rab29-mediated LRRK2 kinase activation using co-IP and quantitative immunoblotting to measure the interaction of LRRK2 and Rab29 in the presence of TRIM1 constructs (WT, C, and ΔRF) or control vector. Intriguingly, TRIM1 constructs with retained E3 ligase function (WT, C) increased co-IP of Rab29 with WT LRRK2 relative to control vector, while TRIM1 ΔRF did not (Fig. 8 b, quantified in Fig. 8 c, middle panel). LRRK2 R1441G showed the same trend, although the findings did not reach significance using nonparametric multiple comparison testing. Interestingly, Rab29 coimmunoprecipitated with LRRK2 showed the same pattern of Thr71 phosphorylation as total (lysate) Rab29, with the fraction of phosphorylated Rab29 decreased in the presence of TRIM1 WT and TRIM1 C but not in the presence of TRIM1 RF (Fig. 8 c, bottom panel). While further work is required to delineate the precise mechanisms by which TRIM1 can inhibit Rab29-mediated LRRK2 activation, these findings suggest that E3-ligase active TRIM1 can modulate the interaction of Rab29 and LRRK2. One possible mechanism is that ubiquitination changes the binding properties of LRRK2 to Rab29, stabilizing their association in a conformation that blocks Rab29 phosphorylation.

TRIM1 rescues the neurite outgrowth defect caused by LRRK2 G2019S

The most common LRRK2 PD-driving point mutation is LRRK2 G2019S. LRRK2 G2019S expression reproducibly causes decreased neurite outgrowth, a microtubule-driven process that reflects neuronal health (MacLeod et al., 2006; Sheng et al., 2012). Similar to WT LRRK2, LRRK2 G2019S was drawn to microtubules in H1299 cells (Fig. 9 a), ubiquitinated (Fig. 9 b), and degraded via the proteasome (Fig. 9 c) in HEK-293T cells in a TRIM1-dependent manner. To test if TRIM1 rescues LRRK2 G2019S-driven neurite outgrowth deficits, we used a previously published rat PC12 pheochromocytoma cell line harboring dox-inducible LRRK2 G2019S (PC12 dox-LRRK2 G2019S;

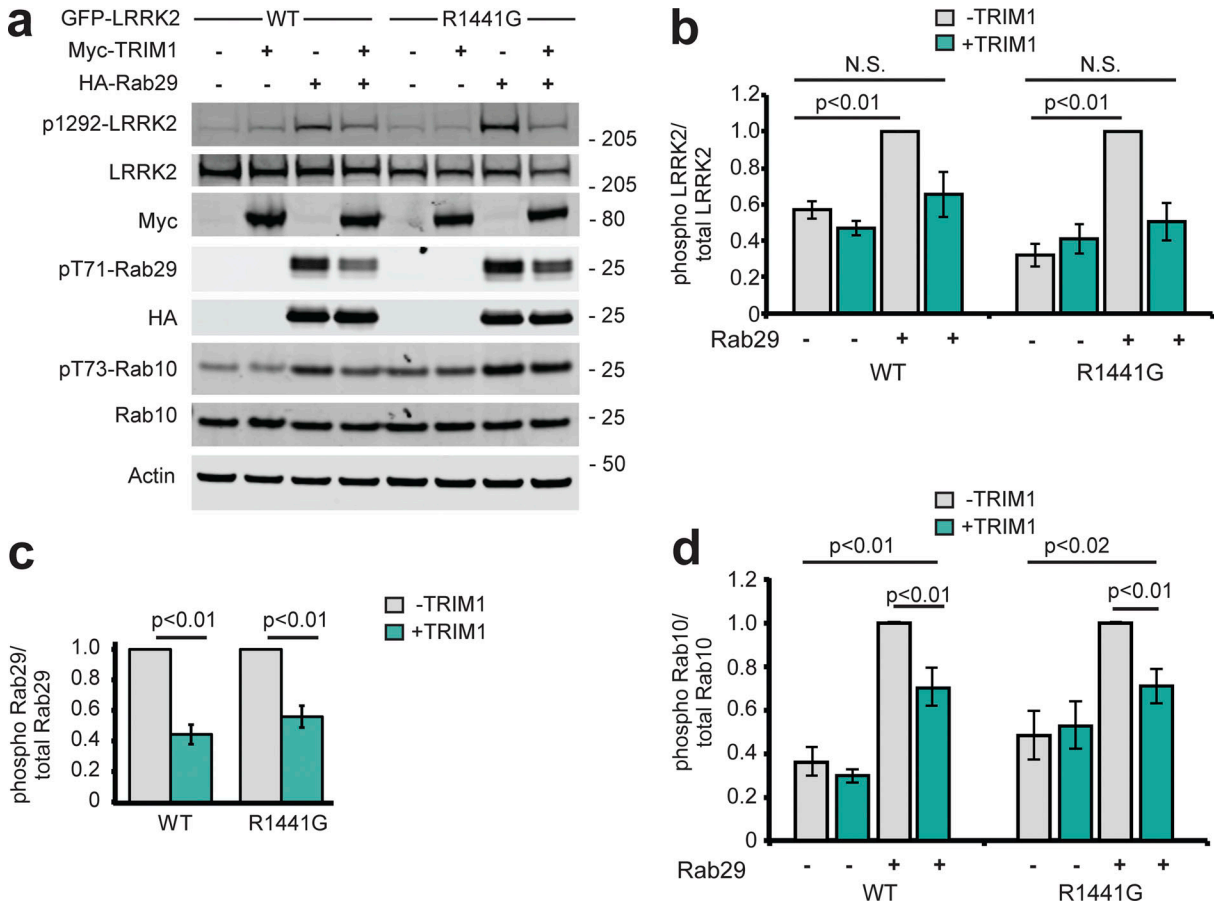

Figure 7. **TRIM1 decreases LRRK2's activation by Rab29. (a)** Immunoblot of LRRK2 phosphorylation at Ser1292, Rab29 phosphorylation at Thr71, and Rab10 phosphorylation at Thr73 in the presence and absence of TRIM1 for WT LRRK2 and LRRK2-PD mutant R1441G. **(b)** Quantification of LRRK2 autophosphorylation in panel a. **(c)** Quantification of Rab29 Thr71 phosphorylation in panel a. **(d)** Quantification of Rab10 Thr73 phosphorylation in panel a. Quantifications show the mean value from three to four independent replicates, with error bars showing SEM. Significance testing for b–d was performed using Kruskal–Wallis with post hoc Dunn test and Bonferroni correction. Source data are available for this figure: SourceData F7.

Migheli et al., 2013). We validated that type 1 LRRK2 kinase inhibitors rescue the neurite outgrowth deficiency caused by induction of LRRK2 G2019S in this cell line, demonstrating that the phenotype is LRRK2-dependent (not shown) and that TRIM1 caused microtubule localization of GFP-LRRK2 G2019S (Fig. S5 e) and LRRK2 ubiquitination in PC12 cells (Fig. S5 f).

PC12 dox-LRRK2 G2019S cells were transfected with mCherry-TRIM1 or control vector, with and without dox induction, and treated with nerve growth factor for 5 d to induce neurite outgrowth (representative neurons shown in Fig. 9 d). The proportion of cells with neurites (defined as at least one cellular process greater than cell body length; Das et al., 2004) was quantified, as was neurite length. Expression of TRIM1 alone did not affect PC12 neurite outgrowth (49% ± 2% neurite-bearing cells without TRIM1 expression; 46% ± 9% neurite-bearing cells with TRIM1 expression; Fig. 9 e). LRRK2 G2019S induction significantly reduced the proportion of cells with neurite outgrowth, a phenotype that was completely rescued by coexpression of TRIM1 (29% ± 6% neurite-bearing cells with LRRK2 G2019S without TRIM1; 44% ± 6% neurite-bearing cells with LRRK2 G2019S and TRIM1). In cells bearing neurites, expression of TRIM1 without LRRK2 G2019S did not affect neurite length (40.8 ± 3.9 µm without TRIM1 expression; 46.1 ± 8.5 µm with TRIM1 expression; Fig. 9 f). LRRK2 G2019S induction reduced neurite length in the absence of TRIM1, while expression of TRIM1 with LRRK2 G2019S fully rescued neurite length (32.4 ± 3.5 µm with LRRK2 G2019S without TRIM1; 48.7 ± 7.5 µm with LRRK2 G2019S and TRIM1). Thus, in this model, TRIM1 protects against LRRK2 G2019S-induced neurite outgrowth defects, suggesting it could potentially ameliorate LRRK2 neurotoxicity in other systems.

Discussion

Here we show that TRIM1 is a novel LRRK2 binding partner that ubiquitinates both WT and PD-mutant LRRK2 and influences LRRK2 degradation, subcellular localization, and Rab29 binding/kinase activation, as well as countering LRRK2 G2019S's inhibitory effect on neurite outgrowth (Fig. 10). TRIM1 recruits LRRK2 to the microtubule cytoskeleton and drives LRRK2 K48-linked polyubiquitination and proteasomal degradation. Overexpression of TRIM1 decreased levels of overexpressed LRRK2 in cell lines and primary cortical neurons; knockdown and CRISPR

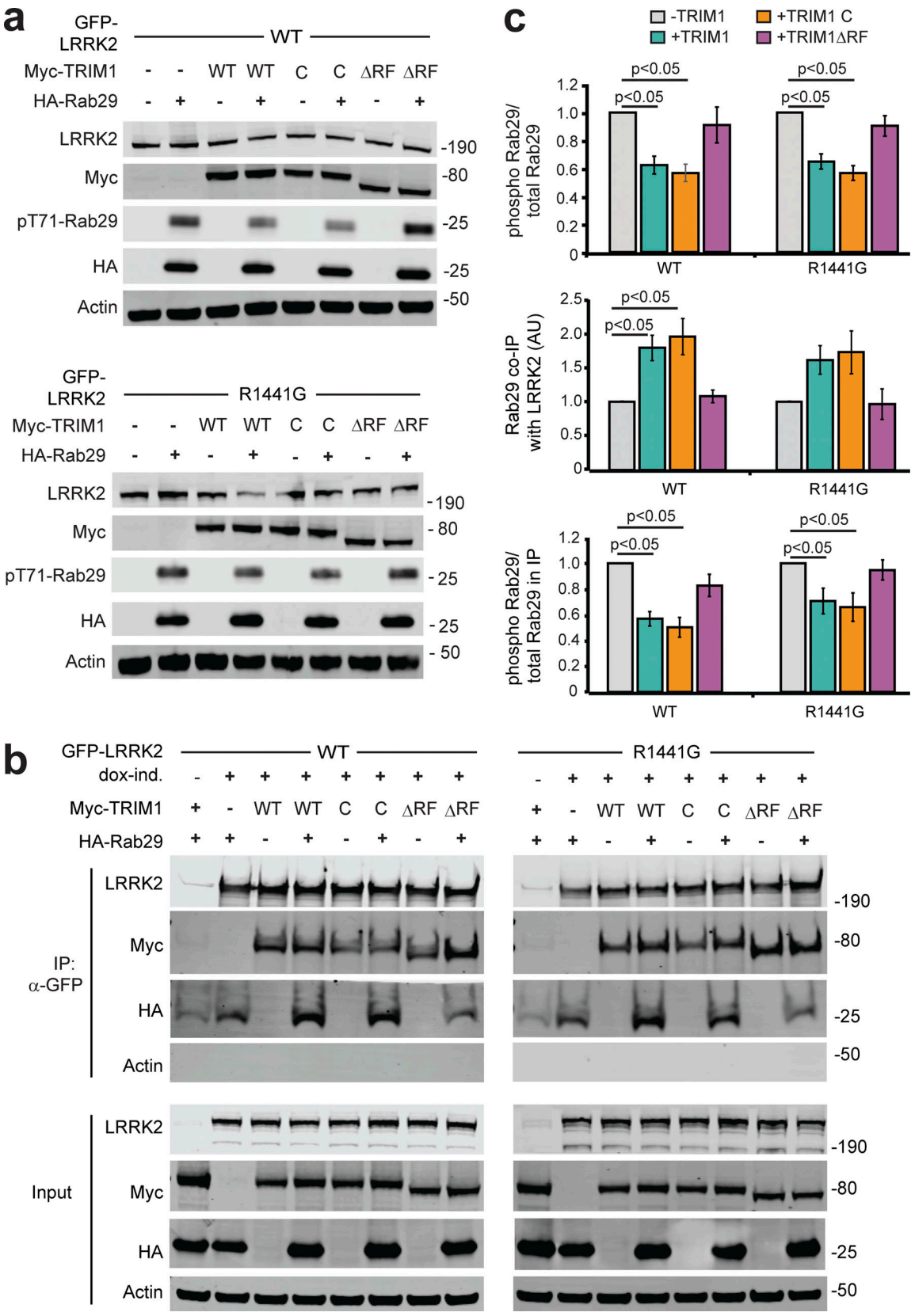

Figure 8. **The LRRK2–Rab29 interaction is modulated by TRIM1's E3 ligase activity. (a)** Immunoblot of Rab29 phosphorylation with WT LRRK2 (top) or LRRK2-PD mutant R1441G (bottom) in the absence of overexpressed TRIM1 or with overexpression of myc-tagged WT TRIM1 (WT), microtubule-nonbinding TRIM1 (TRIM1 C), or TRIM1 lacking E3-ligase function (TRIM1ΔRF). **(b)** Coimmunoprecipitation of Rab29 and TRIM1 variants with LRRK2 WT or R1441G. dox-ind., dox-induced. **(c)** Quantification of: Rab29 phosphorylation relative to total Rab29 in lysate from part A (top panel), Rab29 co-IPed with LRRK2 in the

presence or absence of overexpressed TRIM1 variants from part B (middle panel) and Rab29 phosphorylation relative to total Rab29 in co-IP with LRRK2 in the presence or absence of overexpressed TRIM1 variants (bottom panel). All immunoblots are representative images, and quantification shows the mean value from at least three independent experiments, with error bars showing the SEM. Significance testing for panel c was performed using Kruskal–Wallis with post hoc Dunn test and Bonferroni correction. Source data are available for this figure: SourceData F8.

KO of endogenous TRIM1 increased steady-state levels of endogenous LRRK2. Until now, the ubiquitous protein CHIP was the primary E3 ligase identified to target LRRK2 to the proteasome (Ding and Goldberg, 2009; Edkins, 2015; Ko et al., 2009). We found that TRIM1 drove LRRK2 proteasomal degradation more strongly than CHIP in our flow cytometric assay. CHIP mediates turnover of many unstable proteins (Edkins, 2015) and appears particularly important for degradation of destabilized LRRK2 variants, such as the sporadic-PD risk allele, LRRK2 G2385R (Rudenko et al., 2017). One hypothesis is that CHIP may be especially important in degradation of unstable, misfolded LRRK2, while TRIM1's role in LRRK2 degradation may be related to LRRK2's phosphorylation state and possibly to LRRK2's subcellular localization.

We used domain constructs to identify the regions mediating LRRK2's interaction with TRIM1. TRIM1's B-box domain (particularly B-box 1) was required for LRRK2 binding. $LRRK2_{822–982}$, a 160–amino acid segment of LRRK2 between the ankyrin and LRR domains, was sufficient for TRIM1 to bind and microtubule-localize LRRK2. We used alanine scanning to further define the TRIM1 binding region of LRRK2 and found that only 9 amino acids, $LRRK2_{911–919}$, are required for TRIM1 to bind, ubiquitinate, and bring LRRK2 to the microtubule. Interestingly, $LRRK2_{911–919}$ lies between Ser910 and Ser935, both of which are phosphorylated by upstream kinases to allow LRRK2 to bind 14-3-3 proteins (Muda et al., 2014; Nichols et al., 2010). We found that the LRRK2–TRIM1 interaction can occur in the absence of Ser910/Ser935 phosphorylation, whereas, as others have demonstrated, the LRRK2-14-3-3 interaction requires phosphorylation of LRRK2 Ser910/Ser935. 14-3-3 binding stabilizes LRRK2 in the cytoplasm (Dzamko et al., 2010), whereas TRIM1 binding recruits overexpressed LRRK2 to microtubules. Interestingly, secondary structure modeling predicts $LRRK2_{822–982}$ to be predominantly unstructured, consistent with the recent cryo-EM structure of full-length LRRK2, for which $LRRK2_{853–981}$ could not be solved (Myasnikov et al., 2021). We therefore propose that $LRRK2_{853–981}$ may serve as a regulatory loop whose phosphorylation status, and possibly conformation, may dictate LRRK2's binding to interacting partners. LRRK2's close homolog LRRK1, which has a domain structure very similar to that of LRRK2, lacks the RL region. LRRK1 also contains no mutations linked to PD (Reyniers et al., 2014). We speculate that the RL region may be an important regulator of PD-relevant LRRK2 functions.

Like others, we find that Rab29 overexpression robustly augments WT and PD-mutant LRRK2 kinase function (Purlyte et al., 2018). Intriguingly, TRIM1 inhibits Rab29-mediated LRRK2 kinase activation (for both WT and PD-mutant R1441G LRRK2), and this effect is not due to decreased LRRK2 protein levels. Inhibition requires that TRIM1 contain an intact E3 ligase domain but does not require TRIM1 to bind microtubules, suggesting that ubiquitination but not microtubule-binding drives inhibition. We found that E3-intact TRIM1 augments the interaction between LRRK2 and Rab29, as measured by co-IP. This finding may suggest that ubiquitination of LRRK2 by TRIM1 changes the conformation of LRRK2 and causes LRRK2 to more strongly bind Rab29 in a kinase-inactive conformation. With 60% sequence coverage, we used MS to identify LRRK2 K831 as a site of TRIM1-mediated ubiquitination. However, a LRRK2 K831R mutation did not restore Rab29-mediated LRRK2 kinase activation in the presence of TRIM1. Because LRRK2 is such a large protein, 60% coverage identified 92 of 176 Lys residues but left the ubiquitination state of 84 Lys residues unknown. Thus, other ubiquitination sites or additional E3-driven protein modifications on LRRK2 may be important for regulating the LRRK2-Rab29 interaction. Alternatively, we cannot rule out the possibility that TRIM1 ubiquitination of a non-LRRK2 target modulates the LRRK2-Rab29 interaction. TRIM1 ubiquitination sites on LRRK2 remain to be fully delineated, as does the mechanism by which TRIM1 inhibits Rab29's kinase activation of LRRK2.

This work uncovers the microtubule cytoskeleton as a potential site of LRRK2 turnover, a new role for the cytoskeleton in PD. Multiple groups have reported an association of LRRK2 with microtubules (Godena et al., 2014; Law et al., 2014; Schmidt et al., 2019; Watanabe et al., 2020), including work that solved the structure of the LRRK2-microtubule interface to 14 Å (Watanabe et al., 2020), and a second study that suggests that LRRK2's direct interaction with microtubules is regulated by the conformation of its kinase domain (Deniston et al., 2020). However, the physiologic function of LRRK2's microtubule association has not been rigorously investigated, and some authors have suggested that LRRK2-microtubule filaments represent concentration-dependent aggresomes (Purlyte et al., 2018). We found that TRIM1, but not the highly homologous TRIM18, binds a 9–amino acid segment of LRRK2 to promote endogenous LRRK2 degradation. Although TRIM1 C, a microtubule nonbinding construct, can ubiquitinate LRRK2, all published evidence suggests that endogenous TRIM1 and TRIM18 are entirely localized to microtubules. TRIM1 and TRIM18 are known to ubiquitinate other substrates at microtubules, targeting them for degradation. TRIM1 ubiquitinates astrin, a microtubule-associated protein involved in cell division, to decrease astrin levels and promote cell division (Gholkar et al., 2016). TRIM18 binds α4, a regulatory subunit of protein phosphatase 2a (PP2a), at microtubules, causing ubiquitination and degradation of PP2a (Trockenbacher et al., 2001). Our findings thus support a model in which microtubule association plays a physiologic role in LRRK2 biology.

Interestingly, while mCherry-TRIM1 coats microtubules in a uniform and smooth distribution (Fig. 2 b, left panel, inset), GFP-LRRK2 forms more discontinuous and punctate structures,

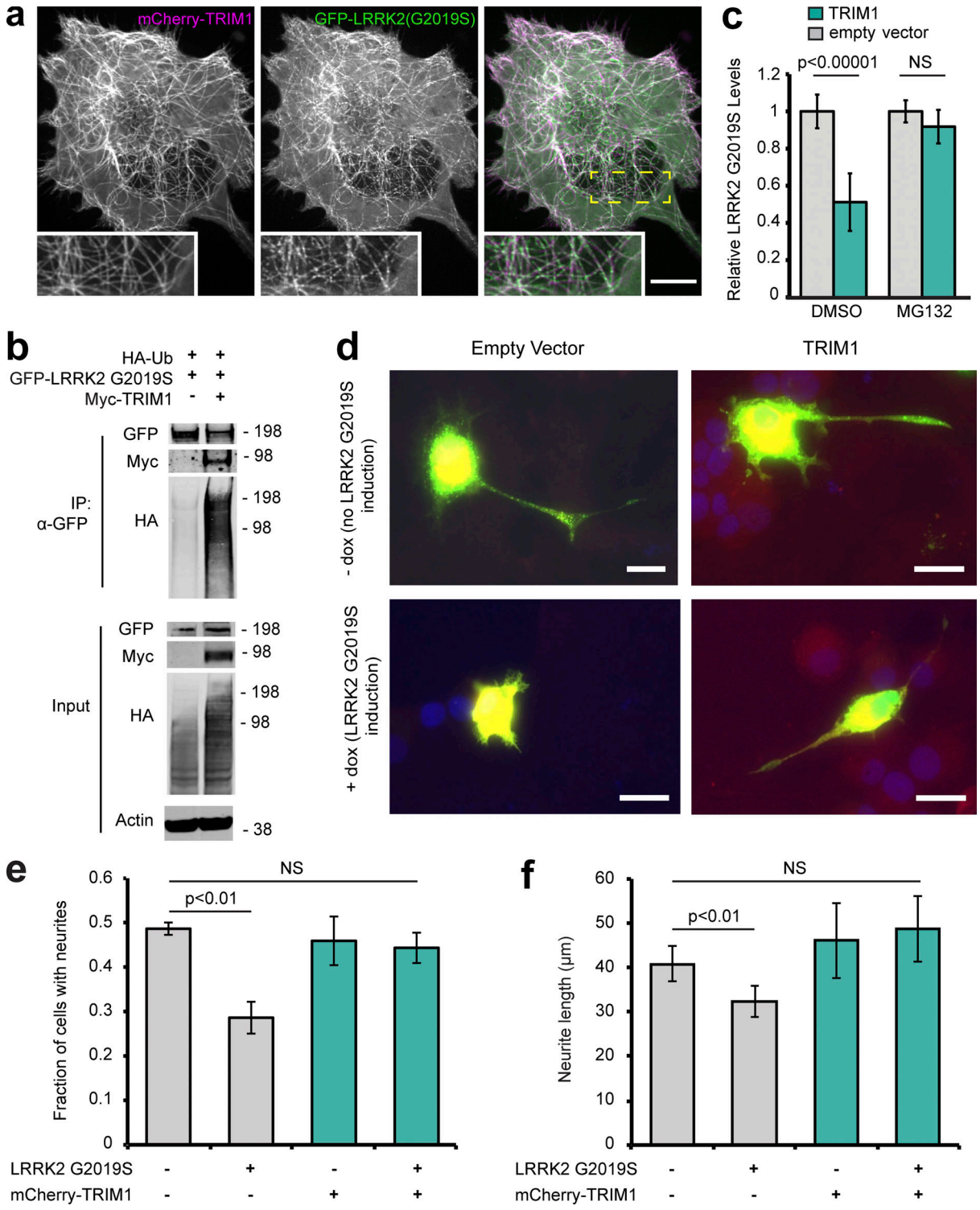

Figure 9. **TRIM1 mediates proteasomal degradation of PD-mutant LRRK2 G2019S to rescue its toxicity. (a)** Live-cell confocal microscopy of GFP-LRRK2 G2019S and mCherry-TRIM1 transiently transfected into H1299 cells. Scale bar = 10 μM. **(b)** Coimmunoprecipitation and ubiquitination (Ub) of GFP-LRRK2 G2019S with myc-TRIM1 in the presence of HA-ubiquitin in HEK-293T cells. **(c)** Flow cytometric assay on dox-inducible GFP-LRRK2 G2019S HEK-293T cells in the presence and absence of TRIM1 and the proteasome inhibitor MG132; bars show median green fluorescence intensity with error bars showing twice the SEM. **(d)** Representative dox-inducible LRRK2 G2019S PC-12 cells transfected with mCherry-TRIM1 or mCherry alone vector and GFP and differentiated with NGF for 5 d in the presence and absence of 1 μg/ml dox. Scale bar = 10 μM. **(e)** Quantification of the fraction of neurite-bearing PC-12 cells in the presence and absence of LRRK2 G2019S and the presence and absence of TRIM1; bars show mean of three independent experiments of 150–250 cells each; error bars show SEM. **(f)** Quantification of average neurite length on PC-12 cells with neurites in the presence and absence of LRRK2 G2019S and the presence and absence of TRIM1; bars show mean of three independent experiments; error bars show SEM. Significance testing for panel c was performed using ANOVA with post hoc *t* test with Bonferroni correction. Significance testing for panel e was performed using a test for equality of binomial parameters, and for panel f, using Kruskal–Wallis with post hoc Dunn test and Bonferroni correction. Source data are available for this figure: SourceData F9.

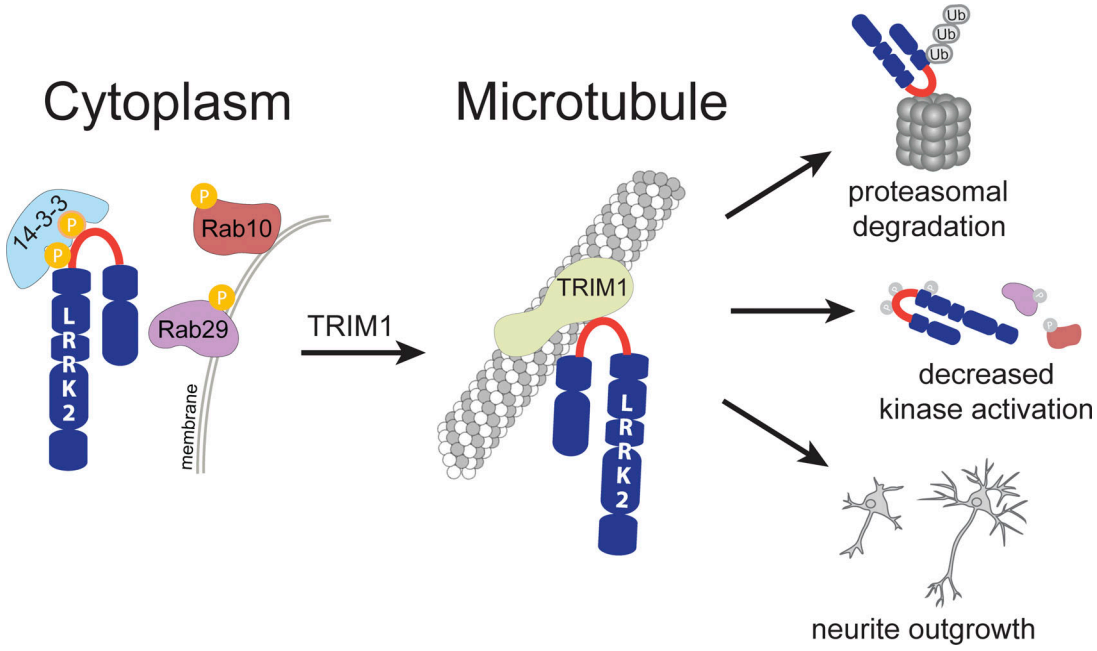

Figure 10. **Model of the LRRK2 RL/TRIM1 interaction.** Schematic highlighting the array of downstream effects of TRIM1 binding LRRK2 RL. The phosphorylation state of S910 and S935 in the RL influences LRRK2's preference for binding 14-3-3 versus TRIM1, which in turn alters LRRK2 localization (cytoplasm versus microtubule), ubiquitination and turnover, kinase activation by Rab29, and neuronal toxicity as measured by neurite outgrowth.

possibly suggestive of multiprotein complexes (Fig. 2 b, middle panel, inset). We predict that, in addition to causing LRRK2 turnover, the association of TRIM1 and LRRK2 at the microtubule cytoskeleton is likely to have additional functions that are yet to be delineated. LRRK2's phosphorylation of Rab8 and Rab10 plays a critical role in ciliogenesis (Dhekne et al., 2018; Steger et al., 2017) and centrosomal cohesion (Lara Ordonez et al., 2019). Cilia and centrosomes are microtubule-based structures, and Rab8- and Rab10-positive vesicles intimately associate with them (Dhekne et al., 2018). One possibility is that endogenous LRRK2 undergoes regulated trafficking between physically proximate Rab-positive membranes, microtubules, and the cytoplasm. Because LRRK2 contains numerous protein–protein interaction domains and has many features of a scaffolding protein, identification of other LRRK2 binding partners at microtubules may provide important insight into additional functions and regulation, as well as potential therapeutic targets.

A limitation of our study is that we were not able to visualize endogenous LRRK2 via confocal microscopy, and all microscopy studies used overexpressed LRRK2. In the cell types used in this work, the low levels of endogenously expressed LRRK2 have prohibited visualization of endogenous LRRK2 by confocal microscopy by any authors. In fact, the only study that we believe definitively identifies endogenous LRRK2 via confocal or other microscopy (Eguchi et al., 2018) used macrophages, which express extremely low levels of TRIM1 (Eguchi et al., 2018; Rajsbaum et al., 2008). This limitation highlights an important roadblock in the field. Ongoing work by our group and others is focused on optimizing LRRK2 CRISPR tags, nanobodies, and other tools to allow definitive localization of LRRK2 and PD-mutant LRRK2.

Finally, TRIM1 falls within the PARK12 genomic locus on the X-chromosome (Pankratz et al., 2003). While it is tempting to speculate that TRIM1 mutations may be linked to PD, PARK12 is a large locus containing ∼600 genes, and much additional work remains to determine if TRIM1 variants increase risk for PD. Regardless, TRIM1 may serve as a novel therapeutic target for PD, as suggested by our data that TRIM1 ameliorates LRRK2 G2019S-mediated neurite outgrowth defects. The mechanism by which LRRK2 G2019S inhibits neurite outgrowth is unknown; however, increases in both LRRK2 kinase activity and protein levels have been linked to neurotoxicity in PD (Di Maio et al., 2018), and we observe that TRIM1 regulates both. More broadly, our studies suggest that cellular pathways decreasing LRRK2 protein levels are possible targets to combat PD and should be identified and tested.

Materials and methods

Cell lines and tissue culture

All cell lines were grown at 37°C in a humidified atmosphere with 5% CO_2. Human HEK-293T cells and human A549 cells were cultured in DMEM with 10% FBS. Dox-inducible GFP-LRRK2 HEK-293T cell lines (Zhao et al., 2015) were cultured in DMEM with 10% tetracycline-free FBS, 10 µg/ml blasticidin, and 100 µg/ml hygromycin. Human H1299 cells were cultured in RPMI 1640 with 10% FBS, 25 mM HEPES, and 2.0 g/liter $NaHCO_3$. Malme-3M cells were grown in RPMI 1640 with 10% FBS and 2 mM (1×) L-alanyl-L-glutamine (GlutaMAX; Thermo Fisher Scientific). SK-N-SH human neuroblastoma cells were cultured in Eagle's minimum essential medium. Rat primary cultures of cortical neurons were created from rat pup cortices

at embryonic days 20–21 and cultured and differentiated as previously described (Skibinski et al., 2017) in neurobasal growth medium with 2 mM GlutaMAX, penicillin/streptomycin, and B27 supplement (NB media). Rat PC-12 cells were grown in DMEM supplemented with 15% tetracycline-free FBS and 2 mM GlutaMAX. Dox-inducible LRRK2 rat PC-12 cell lines (Migheli et al., 2013) were grown in DMEM supplemented with 10% horse serum and 5% tetracycline-free FBS or 15% tetracycline-free FBS, 2 mM GlutaMAX, 100 U/ml penicillin G, 100 µg/ml streptomycin, 400 µg/ml G418, and 200 µg/ml hygromycin and were differentiated under low-serum conditions in the same media containing 1% horse serum without FBS and 100 ng/ml NGF. PC12 cell differentiation medium was replaced every 48 h.

Plasmids

Plasmids pcDNA5 frt/to expressing GFP-tagged human LRRK2, both full-length and truncation and point mutants, and pCMV-C2-6myc or pCMV-C2-EGFP expressing WT human TRIM18 and TRIM1, both full-length and domain mutants, have been previously described (Short et al., 2002; Zhao et al., 2015) as has plasmid V5-14-3-3 θ (Kett et al., 2012). Plasmid expressing mCherry-tubulin was a gift from Roger Tsien (Shaner et al., 2004), and plasmid pRK5-HA-ubiquitin WT was a gift from Ted Dawson (plasmid #17608; Addgene; Lim et al., 2005).

Full-length human LRRK2 with N-terminal myc and FLAG tags was cloned into pcDNA5 frt/to. In brief, pCMV-2myc-LRRK2, a gift from Mark Cookson (plasmid #25361; Addgene; Greggio et al., 2008) was cloned into pcDNA5 frt/to by site-directed mutagenic removal of a single LRRK2 internal HpaI site (Quikchange; Stratagene), followed by HpaI/Eco53KI digestion, ligation into EcoRV site, and return of HpaI site. A 2× FLAG tag was introduced upstream of the 2× myc tag by Quikchange. Addgene plasmid #25361 was found to have the Arg50His variant not present in consensus Uniprot sequence (Q5S007), and site-directed mutagenesis was used to create Arg50.

Plasmid expressing GFP-LRRK2$_{822–982}$ was created by introducing a stop codon in GFP-LRRK2$_{822–2527}$ and plasmids expressing GFP-TRIM1$_{70–119}$ (denoted "linker" Fig. 4 b), GFP-TRIM1$_{70–177}$ (denoted "BB1", Fig. 4 b), and GFPTRIM1$_{70–235}$ (denoted "BB1,2", Fig. 4 b) were created by introducing stop codons into GFP-TRIM1$_{\Delta RF}$. Western blot was used to verify that there was no read-through of the stop codon.

Plasmid expressing mCherry-myc-TRIM1 was created by cloning myc-TRIM1 into pmCherry-C1 (Clontech). Plasmid expressing EBFP2-14-3-3 θ was created using HiFi Cloning (NEB) of 14-3-3 θ into pEBFP2-C1 (plasmid #54665; Addgene). A CHIP plasmid (Petrucelli et al., 2004) was a gift from Leonard Petrucelli, and the CHIP ORF was cloned into pCMV-C2-6myc. Eos3.2-LRRK2 and mApple ORFs were synthesized and cloned into pGW1. All constructs were verified by DNA sequencing.

Antibodies

The following antibodies were used: mouse anti-LRRK2 (N241A/34; 75-253; Neuromab), rabbit anti-LRRK2 (C41-2; ab133474; Abcam), rabbit anti-phospho-Ser910 LRRK2 (UDD 1 15(3); ab133449; Abcam), rabbit anti-phospho-Ser935 LRRK2 (UDD2 10(12); ab133450; Abcam), rabbit anti-phospho-Ser1292 LRRK2 (ab203181; Abcam), rabbit anti-FLAG (F7425; Sigma-Aldrich), mouse anti-myc (clone 9E10, M4439; Sigma-Aldrich), rabbit anti-myc (clone 71D10, 2278; Cell Signaling), rabbit anti-mCherry (ab167453; Abcam), rabbit anti-TRIM1 (M2448; Sigma-Aldrich; PA5-28457; Thermo Fisher Scientific), mouse anti-GFP (clone GF28R, MA5-15256; Thermo Fisher Scientific), rabbit anti-HA (clone C29F4, 3724S; Cell Signaling), mouse anti-HA (H3663; Sigma-Aldrich), mouse anti-V5 (clone E 10/V4RR, MA5-15253; Thermo Fisher Scientific), mouse anti-Rab10 (Sab5300028; Sigma-Aldrich), rabbit anti-phospho-Thr71 Rab29 (ab241062; Abcam), rabbit anti-phospho-Thr73 Rab10 (ab230261; Abcam), mouse anti-ubiquitin (MAB1510-I; Millipore Sigma; P4D1, sc-8017; Santa Cruz), rabbit linkage-specific K63 anti-ubiquitin (ab179434; Abcam), rabbit linkage-specific K48 anti-ubiquitin (4289; Cell Signaling), rabbit anti-actin (clone 13E5, 4970; Cell Signaling), and mouse anti-actin (A1978; Sigma-Aldrich). For Western blot, all primary antibodies were used at 1:250 to 1:1,000 dilution except actin (1:1,000 to 1:5,000), and secondary antibodies (IRDye 800CW or 680RD goat anti-mouse or anti-rabbit IgG; LI-COR) were used at 1:10,000 dilution. Where appropriate, immunoblot membranes were physically cut to allow for a single set of samples to be exposed to multiple primary antibodies at distinct epitope-containing regions (i.e., different molecular weights). For chemiluminescence of immunoblots, secondary antibodies used were peroxidase-conjugated AffiniPure donkey anti-mouse (715-035-150; Jackson ImmunoResearch) and peroxidase-conjugated donkey anti-rabbit (711-035-152; Jackson ImmunoResearch), with SuperSignal West Femto Maximum Sensitivity Substrate (34094; Thermo Fisher Scientific). For immunoprecipitation and co-IP, the following preconjugated agarose-resin systems were used according to manufacturer instructions: anti-FLAG M2 (A2220; Sigma-Aldrich); GFP-trap_A or magnetic GFP-trap_MA, myc-trap_A or magnetic myc-trap_MA or mCherry-trap_A (Chromotek); Pierce anti-HA (Thermo Fisher Scientific), magnetic anti-V5 beads (MBL International), and magnetic bead–conjugated panselective TUBE2 (UM402M; LifeSensors). Anti-TRIM1 antibodies were conjugated to magnetic Dynabeads following manufacturer's instructions (Invitrogen).

Cell transfection, drug treatment, and lysis

HEK-293T cells were transfected using Fugene 6 (Promega), Lipofectamine LTX, or Lipofectamine 2000 (Thermo Fisher Scientific); H1299 cells were transfected with Lipofectamine 2000; and PC12 cells were transfected with Lipofectamine LTX or Lipofectamine 3000, all per manufacturer's instructions. LRRK2 expression was induced with 2 ng/ml to 1 µg/ml dox. The proteasomal inhibitor MG132 was used at 2 µM for 24 h. Autophagy was inhibited with chloroquine at 25 µM for 24 h. LRRK2 kinase inhibitor MLi-2 was used at 100–200 nM for 24 h for protein turnover assays and 4 h for colocalization studies, and at 500 nM for 5 h for co-IP studies. Proteasome inhibitor bortezomib was used at 1–100 nM for 8–18 h. For cell lysates, cells were harvested by scraping or trypsinization, pelleted, washed with PBS 2×, lysed either by pipetting up and down or by homogenization using a pellet pestle (Kimble Scientific) in 1 ml

ice-cold immunoprecipitation buffer (50 mM Tris, pH 7.5, 150 mM NaCl, 1 mM EDTA, and 0.5% NP-40) supplemented with cOmplete protease inhibitor (11836170001; Roche) and Phosstop phosphatase inhibitor (04906845001; Roche), and rotated end-over-end at 4°C for 30 min. Debris was pelleted at 10,000–15,000 rcf for 5 min at 4°C. Lysate total protein concentration was measured using the Pierce BCA Protein Assay Kit (23225; Thermo Fisher Scientific).

For rat cortical neurons, at 3–4 d in vitro, neurons were transfected with plasmids and Lipofectamine 3000. Before adding the lipofectamine-DNA mix, cells were incubated in Neurobasal with 1× KY media (10 mM kynurenic acid, 0.0025% phenol red, 5 mM Hepes, and 100 mM $MgCl_2$). Primary neurons were incubated in lipofectamine-DNA mix for 20–40 min, washed with Neurobasal, and cultured in NB medium.

Immunoprecipitation, MS, and data analysis of LRRK2 interactome

6 µg of either pcDNA5 containing the above FLAG-LRRK2 construct or FLAG tag alone was transfected into 15-cm dishes of HEK-293T cells using Fugene 6. Cells were harvested 48 h after transfection using 10 mM EDTA in D-PBS for 5 min at 25°C, followed by two PBS washes. Cells were lysed as above, with protein concentrations normalized by bicinchoninic acid (BCA) assay, and the resulting lysates incubated with 30 µl anti-FLAG M2 (A2220; Sigma-Aldrich) preconjugated agarose-resin for 2–3 h at 4°C. FLAG affinity purification followed by MS was carried out essentially as described in Jager et al. (2011) except that 100 µg/ml FLAG peptide was used to elute bound proteins (F3290; Sigma-Aldrich; Jager et al., 2011). In brief, after elution, 10 µl of the IP eluate was reduced with 2.5 mM DTT at 60°C for 30 min followed by alkylation with 2.5 mM iodoacetamide for 40 min at room temperature. 100 ng sequencing grade modified trypsin (Promega) was added to the sample and incubated overnight at 37°C. Peptides were then desalted on ZipTip C18 pipette tips (Millipore), lyophilized to dryness, and resuspended in a final solution of 0.1% formic acid for injection into a Thermo Fisher Scientific LTQ Orbitrap XL Mass Spectrometer. For affinity purification–MS experiments, raw data conversion and Protein Prospector search were performed as described previously (Jager et al., 2011).

Genome editing of TRIM1

CRISPR-Cas9 mediated KO of the TRIM1 genomic locus in HEK-293T cells was performed essentially as described (Ran et al., 2013). Specifically, a sgRNA targeting the N-terminus of TRIM1's RING domain (5′-CAACTCTAGGCAGATTGGAC-3′) with low off-targeting score was chosen following careful transcript analysis using NCBI and the Zhang lab CRISPR Design tool (https://crispr.mit.edu). Complementary dsDNA oligos with BbsI-compatible overhangs were designed, dsDNA guide inserts were ligated into BbsI-digested pSpCas9(BB)-2A-GFP (PX458; plasmid #48138; Addgene), and plasmids were verified by sequencing. 40 h before transfection, HEK-293T cells were seeded at 4 × 10^5 cells per 35-mm well. Transfection of 2.5 µg PX458/sgRNA was performed using Lipofectamine 3000. 24–48 h after transfection, cells were harvested, and GFP-positive cells were isolated using a BD FACSAria II and grown in DMEM supplemented with 10% FBS. After 2 wk, GFP-negative cells were single-cell sorted (BD FACSAria II) into 96-well plates, and single clones were expanded. After reaching ∼80% confluency, individual clones were transferred into 6-well plates and then expanded further, and genomic DNA was harvested as below.

For genetic verification of KOs, genomic DNA was isolated using a KAPA Mouse Genotyping Kit (Roche). PCR amplification of the N-terminal region of TRIM1 was performed using Q5 High-Fidelity 2× Master Mix (New England BioLabs; primers: forward, 5′-TGTGTTCAGCACAGAAATGCCT-3′; reverse, 5′-AGG CAGGCTTAGAATTAGCCC-3′) and cloned into the TOPO TA cloning kit (Thermo Fisher Scientific), and single colonies were sequenced. For each cloning reaction, DNA was isolated from more than eight bacterial colonies using QIAprep Spin Miniprep Kit (Qiagen), and TRIM1 KO was confirmed by sequencing using a T3 forward promoter to confirm truncating stop codons in all copies of the TRIM1 gene present in the genome of selected clones. Isolation of genomic DNA and sequencing from the parental WT HEK-293T cell line was performed in parallel and demonstrated WT alleles of TRIM1 as expected. Absence of endogenous TRIM1 protein was confirmed using immunoprecipitation with anti-TRIM1 antibodies conjugated to Dynabeads, followed by immunoblotting for TRIM1 in parallel to the positive-control parental WT cells (Fig. 1 e; see Immunoprecipitation below).

Immunoprecipitation and co-IP

Cells were lysed in immunoprecipitation buffer as above, and lysate protein concentrations were quantified by BCA and normalized before addition of 20–40 µl antibody-conjugated beads (GFP, myc, HA, or V5, listed above, or Dynabead-conjugated anti-TRIM1). Immunoprecipitations were performed at 4°C for 2–12 h. Beads were washed ≥3× in wash buffer (50 mM Tris, pH 7.5, 150–500 mM NaCl, and 1 mM EDTA), and bound proteins were eluted by heating at 70–95°C in 40–80 µl 4× NuPage LDS loading buffer with 5% β-mercaptoethanol. Samples were run on NuPage Novex minigels, either 4–12% Bis-Tris or 3–8% Tris-acetate, and transferred onto PVDF membrane with the Genscript eBlot L1 transfer system and blocked with LI-COR Intercept TBS blocking buffer. All imaging and quantification of immunoblots was performed using a LI-COR Odyssey CLx imaging system and Image Studio Lite software v5.2. All quantification of LRRK2 or phospho-LRRK2 protein levels was performed using 3–8% Tris-acetate gels.

Quantification of LRRK2 protein levels in TRIM1 CRISPR KO

WT HEK-293T and TRIM1 KO CRISPR HEK-293T cells were seeded at 3 × 10^6 cells per plate on 10-cm plates. After 24 h, cells were harvested and lysed in immunoprecipitation buffer (50 mM Tris, pH 7.5, 150 mM NaCl, 1 mM EDTA, and 0.5% NP-40) supplemented with cOmplete protease inhibitor (Roche) and Phosstop phosphatase inhibitor (Roche). Cells were lysed by pipetting, and cell lysates were rotated at 4°C for 30 min, and debris was pelleted at 4°C at 5,000 rpm for 10 min. Protein levels in the lysates were normalized by BCA, and samples were run on a Tris-acetate gel at 100 V for 110 min.

Isolation of endogenously ubiquitinated LRRK2 using TUBEs

HEK-293T cells were seeded in 10-cm dishes and transfected with FLAG-LRRK2 in the presence of myc-TRIM1 or myc-alone vector control. After transfection for 8 h, cells were treated with 100 nM bortezomib for 12 h. 20 h after transfection, cells were lysed as above, and lysate protein concentrations were normalized using BCA assay. FLAG-LRRK2 immunoprecipitation was performed using 30 µl FLAG antibody-conjugated beads (Sigma-Aldrich) at 4°C for 1 h. FLAG-LRRK2 was eluted by incubation with 100 µg/ml 3× FLAG peptide at 4°C for 1 h. 50 µl TUBE2 magnetic beads (LifeSensors) was washed 3× in TBS-T, added to eluted FLAG-LRRK2, and rotated at 4°C overnight. TUBE2 beads were washed 3× (50 mM Tris, pH 7.5, 250 mM NaCl, 0.2% NP-40, and 1 mM DTT), and bound proteins were eluted by heating at 70°C for 10 min in 20 µl 4× Nupage LDS loading buffer (NP0007; Invitrogen) containing 5% β-mercaptoethanol. Standards used were K48- and K63-linked recombinant polyubiquitin chains (R&D Biosystems).

LRRK2 siRNA knockdown and co-IP with endogenous TRIM1

800 nM of either LRRK2 siRNA (M-006323-02-0010; Dharmacon) or control scrambled siRNA (D-0001206-13-05) was electroporated into HEK-293T cells according to the Lonza Kit V protocol. After 48-h growth at 37°C, cells were harvested and lysed as above for co-IP. Antibody-conjugated Dynabeads (50 µl; 14311D), previously coupled to TRIM1 antibody (PA5-28457; Thermo Fisher Scientific) or IgG isotype control (550326; BD Pharmingen), were incubated with lysates for 16 h at 4°C. Samples were washed, eluted, and immunoblotted as above.

Live-cell confocal imaging

Cells were seeded onto poly-D-lysine–coated glass-bottom 35-mm dishes (MatTek Corp.), with media and transfection conditions as described above. Spinning disk and laser scanning confocal live-cell imaging was performed under environmentally controlled conditions, at 37°C and 5% CO_2. For experiments using the spinning disk microscope, the protocol is as described in Stehbens et al. (2014) except that the system was upgraded with a next-generation scientific CCD camera (cMyo, 293 Photometrics) with 4.5-µm pixels, allowing optimal spatial sampling using a 60× NA 1.49 objective (CFI 294 APO TIRF; Nikon). For experiments using the Olympus Fluoview 1000 laser scanning confocal microscope, a 60× oil-immersion objective with NA 1.42 was used to obtain confocal images (1,024 × 1,024 pixels). Z-stack images were acquired with a step size of 0.5–1 µm and processed using the Fiji software package.

Quantification of microtubule-bound LRRK2

H1299 cells were seeded at a density of 4 × 10^5 cells per plate on 35-mm glass-bottom dishes (MatTek) and transfected with indicated plasmids using Lipofectamine 2000. 24 h after transfection, live-cell imaging was performed under environmentally controlled conditions, at 37°C and 5% CO_2. Cells were imaged at 60× using either a Nikon Eclipse Ti Fluorescence microscope or an Olympus Fluoview 1000 laser scanning confocal microscope, using a 60× oil-immersion objective. Cells were selected for analysis only if they fluoresced in both the red and green channels and expressed TRIM1 or tubulin at microtubules. Each cell was categorized based on whether LRRK2 localized to microtubules, with the reviewer blinded to the construct transfected. 50 cells were counted per plate, with two plates per transfection condition, for a total of 100 cells per experiment. This was repeated for a total of three independent experiments. For each condition, the number of cells per replicate with LRRK2 localized at microtubules was averaged and expressed as a percentage; error was calculated as SD.

Flow cytometry

GFP-LRRK2 levels were measured in dox-inducible cell lines on a Fortessa flow cytometer (BD Biosciences). Cells were induced with 2–5 ng/ml dox, and dox was washed from cells 18–72 h before analysis. On the day of analysis, cells were trypsinized, pelleted, and washed before being resuspended in DPBS. GFP intensity was measured using a 488-nm laser for excitation and a detector with a 505-nm long-pass filter and a 525/50-nm bandpass filter. Only live, single cells, as determined by forward and side scatter, were analyzed.

CRISPRi knockdown of TRIM1

Catalytically dead Cas9 (dCas9-BFP) was inserted randomly into dox-inducible GFP-LRRK2 HEK-293T cells via lentiviral transduction. Cells were sorted for a BFP^+ pure population on an Aria2SORP. BFP intensity was measured using a 405-nm laser for excitation and a detector with a 450/50-nm bandpass filter. The top four predicted guide RNAs for TRIM1 based on Horlbeck et al. (2016) (5′-GGGGCAGCACCATGACACCA-3′, 5′-GCTCCG GTCACTCCTGCCAG-3′, 5′-GCCCCCAGCCCTTCCTCTGG-3′, and 5′-GCATGTAAACGTGCCTCCAG-3′) were packaged with lentiviral vectors, added to cells, and then puromycin selected (0.75 µg/ml) for 2 d before cells were plated and induced for included experiments. Knockdown was measured via real-time quantitative PCR with a nontargeting gRNA (5′-CCAAGGTAGCATTGG TCTGT-3′) used as a control.

siRNA knockdown of TRIM1

800 nM of either TRIM1 siRNA (L-006938-00-0005; Dharmacon) or control scrambled siRNA (D-0001206-13-05) was electroporated into Malme-3M cells according to the Lonza Kit V protocol. After 24-h incubation, cells were harvested, and RNA was extracted following the NucleoSpin RNA Plus kit protocol (Macherey-Nagel) for qPCR. A TaqMan Gene Expression Assay probe against TRIM1/MID2 (Life Technologies Corp.) was used to confirm the knockdown of TRIM1 mRNA. After 48 h, a parallel replicate of each knockdown was harvested, lysed, and immunoblotted for LRRK2 to measure the effect of TRIM1 knockdowns on LRRK2 protein levels. Protein levels were visualized using two antibodies against LRRK2, C41-2 and N241.

Identification of ubiquitinated LRRK2 lysines by MS

HEK293T cells were seeded in a 15-cm cell culture dish and transfected with FLAG-LRRK2 and HA-ubiquitin plasmids in the presence of myc-TRIM1, myc-ΔRF TRIM1, or myc alone vector control. Sequential immunoprecipitation for FLAG and HA were performed on lysates as described above. Protein samples were

subsequently reduced, alkylated, and digested with trypsin overnight at 37°C. Peptides were then desalted on C18 ziptip columns, lyophilized to dryness, and resuspended in 0.1% formic acid for injection into an Orbitrap Fusion Lumos Tribrid Mass Spectrometer. Raw data were analyzed with MaxQuant to identify and quantify LRRK2 ubiquitination at K831, as well as ubiquitin chain abundance (Brademan et al., 2019). Quantification across samples was normalized by LRRK2 protein abundance.

LRRK2 turnover assay with robotic microscope imaging system

Primary rat cortical neurons in 96-well plates were cotransfected with pGW1-GFP and pGW1-mEos3.2-LRRK2, and either TRIM1 or control plasmid. To measure the degradation of LRRK2 neurons expressing pGW1-GFP, pGW1-Eos3.2-LRRK2 and either TRIM1 or empty vector were photoswitched with a 5–8-s pulse of light at 405-nm wavelength 30–36 h after transfection. Before photoswitching, neurons transfected with mEos3.2-LRRK2 only fluoresce green, with no detectable red fluorescence; upon photoswitching, however, a population of the green protein is irreversibly switched to emit red fluorescence. We then imaged the cells for red fluorescence (mEos3.2-LRRK2-red) every 4–10 h for the next 2 d. Custom-based automated algorithms were used to capture images of neurons in each group in a high-throughput and unbiased manner. Live transfected neurons were selected for analysis based on pGW1-GFP fluorescence intensity and morphology. Neurons were selected only if they had extended processes at the start of the experiment. The abrupt loss of pGW1-GFP fluorescence was used to estimate the survival time of the neuron (Arrasate et al., 2004; Skibinski et al., 2017). The Eos3.2-LRRK2 red fluorescence intensity was measured in each individual neuron at each time point that it was alive, using a region of interest that corresponded to the cell soma. The cotransfected pGW1-GFP provided the morphology mask for the cell soma.

Measurement of phosphorylation in the presence of Rab29 and TRIM1

Dox-inducible GFP-LRRK2 HEK-293T cell lines were cultured as above on 60-mm dishes and transfected at 70% confluency with 0.5 µg plasmid expressing myc-TRIM1 and/or 0.5 µg plasmid expressing HA-Rab29 for 6 h using Lipofectamine 2000. After 6 h, the transfection medium was removed and replaced with medium containing 1 µg/ml dox. Cells were incubated in dox-containing media for 18 h, harvested, and lysed as above. Lysate total protein concentrations were measured by BCA, and 30 µg of lysate per sample was analyzed by immunoblotting. Gel electrophoresis, transfer, immunoblotting, and quantification were performed as described above.

PC12 neurite outgrowth assay

Dox-inducible LRRK2 G2019S PC12 cells were plated at 20,000 cells/well in 96-well plates and transfected with pmaxGFP at 30 ng/well (for analysis of cell morphology) and mCherry-TRIM1 or mCherry empty vector at 200 ng/well. 24 h after transfection, cells were moved to poly-D-lysine–coated coverslips (Neuvitro) in the presence and absence of 1 µg/ml dox. 48 h after transfection, medium was changed to PC12 differentiation medium ±1 µg/ml dox. Cells were then grown in differentiation medium for 5 d, with medium changed every 48–60 h. Cells were then fixed in 4% paraformaldehyde-PBS for 20 min; washed 3× with PBS; permeabilized in PBS with 10% goat serum, 0.4% Triton X-100, 30 mg/ml BSA, and 10 mg/ml glycine for 1 h; washed 3× with PBS; and mounted on slides using Vectashield hardmount with DAPI. All steps from fixation to mounting were performed at 25°C. Cells were imaged at 40× using a Keyence BZ-X700 fluorescence microscope; all cells containing both red and green fluorescence were imaged. The presence/absence of neurites and length of neurites were assessed using ImageJ. Dead cells were excluded from further analysis.

Quantification and statistical analysis

Statistical analysis

General statistical analysis was performed using Excel, R, Python, or STATA. For analysis of flow cytometry data, significance was evaluated using either an unpaired, two-tailed Student's *t* test for two-sample comparisons or ANOVA with post hoc *t* test and Bonferroni correction for three or more groups. For data for which normality could not be assumed, nonparametric testing was used, either the Mann–Whitney *U* test for two-sample comparison or Kruskal–Wallis followed by post hoc Dunn test with Bonferroni correction for multiple comparisons. To test the effect of TRIM1 on the presence or absence of neurite outgrowth, we modeled the proportion of cells with neurites using a binomial distribution (which approximates a normal distribution at our sample size) and tested the null hypothesis that the groups had the same probability of having neurites using a Z-test with Bonferroni correction. A P value < 0.05 was considered statistically significant.

Proteins were identified using Protein Prospector, and high-confidence protein interactions were identified by label-free quantification of bait samples compared with empty vector control using MSstats R-package (Choi et al., 2014). Two independent experiments with two or three independent replicates of WT FLAG-LRRK2 compared with FLAG empty vector were included in the analysis. In the case of rare proteins in which peptides were seen in the presence of LRRK2 but none were identified in the empty vector control, a Mann–Whitney *U* test incorporating additional MS runs was performed to identify proteins significantly increased in the LRRK2 sample.

Flow cytometry data were analyzed using FlowJo software. Data represent the normalized median green fluorescence intensity and twice the SEM.

To measure the degradation of LRRK2 in the robotic microscope imaging system, red-LRRK2 fluorescence was measured longitudinally in each cell for ≥48 h or until death. The red-LRRK2 intensity values from each cell were fitted to an exponential and used to derive a LRRK2 half-life value. Cells were excluded from the analysis if the red-LRRK2 intensity values were lower than local background intensity. Cells without a monotonic decrease in red-LRRK2 signal or with a half-life longer than 3 SDs from the mean were also excluded. The

majority of these excluded cells were due to out-of-focus images. ANOVA was used to compare significant differences between mean half-lives across the groups.

Online supplemental material

Fig. S1 shows additional characterization of the LRRK2-TRIM1 interaction. Fig. S2 shows evaluation of LRRK2 levels and validation of the flow cytometric system to measure LRRK2 turnover. Fig. S3 shows LRRK2 ubiquitination by TRIM1. Fig. S4 shows that TRIM1 binds LRRK2-RL to cause LRRK2 microtubule localization. Fig. S5 shows additional characterization of effects of TRIM1 on LRRK2. Table S1 is related to Fig. 1 and lists LRRK2 interacting partners identified by MS. Table S2 is related to Fig. 3 and lists LRRK2 peptides and ubiquitination sites identified by MS. Video 1 is related to Fig. 2 and shows a time-lapse of GFP-LRRK2 localization in the presence of mCherry-TRIM1 (frame rate is 15 frames/sec).

Data availability

The authors declare that the data supporting the findings of this study are available within the paper and its supplementary information files. Requests for further information and resources and reagents should be directed to and will be fulfilled by the lead contact, Annie Hiniker (ahiniker@health.ucsd.edu).

Acknowledgments

We thank Dario Alessi for use of his CRISPR-edited GFP-LRRK2 A549 cell line, Daniela Boassa for her assistance with confocal microscopy, David Coughlin and Michael Perry for assistance with statistical analyses, and Alexandra Unapanta for critical review of the manuscript.

This work was made possible with support from the UCSF Parnassus Flow Cytometry Core (RRID:SCR_018206) and DRC center grant NIG P30 DK063720, RF1 AG058476 (S. Finkbeiner), P01 AG054407 (S. Finkbeiner), R01 NS124848 (S. Finkbeiner), the Michael J Fox Foundation (S. Finkbeiner), the Taube Koret Center for Neurodegenerative disease (S. Finkbeiner), Laurel Endowment for Pediatric Craniofacial Research (T.C. Cox), the Stowers Family Endowed Chair for Dental & Mineralized Tissue Research (T.C. Cox), Michael J. Fox Foundation LRRK2 Challenge 2014 ID9550 (C. Iaccarino), Fondazione Banco di Sardegna grant number 2014.0489 (C. Iaccarino), Fondo di Ateneo per la ricerca 2020 (C. Iaccarino) and Fondo di Ateneo per la ricerca 2020 (C. Crosio), S10 RR026758 (T. Wittmann), National Institutes of Health R01EY027810 (S.A. Oakes), National Institutes of Health R01CA219815 (S.A. Oakes), National Institutes of Health K08NS090633 (A. Hiniker), DoD W81XWH-18-1-0376 (A. Hiniker), and the American Federation for Aging Research (A. Hiniker).

S. Finkbeiner is on the scientific advisory boards of Foresite Capital and Foresite Laboratories (San Francisco, CA), PurMinds Neuropharma (Toronto, ON), and Origami Therapeutics (San Diego, CA). S.A. Oakes is a founder, equity holder, and consultant for OptiKIRA, LLC (Cleveland, OH) and a consultant for Kezar Life Sciences (South San Francisco, CA). The authors declare no further competing financial interests.

Author contributions: Conceptualization: A.E.D. Stormo, G. Skibinski, N.J. Krogran, S.A. Oakes, A. Hiniker; Data curation: A.E.D. Stormo, F. Shavarebi, G. Skibinski, A. Hiniker; Formal analysis: A.E.D. Stormo, F. Shavarebi, G. Skibinski, A. Hiniker; Funding acquisition: C. Iaccarino, T. Wittmann, S. Finkbeiner, N.J. Krogan, S.A. Oakes, A. Hiniker; Investigation: A.E.D. Stormo, F. Shavarebi, M. FitzGibbon, E.M. Earley, H. Ahrendt, L.S. Lum, E. Verschueren, D.L. Swaney, G. Skibinski, A. Ravisankar, J. van Haren, E.J. Davis, J.R Johnson, J. Von Dollen, C. Balen, J. Porath, C. Crosio, A. Hiniker; Methodology: A.E.D. Stormo, F. Shaverebi, M. FitzGibbon, H. Ahrendt, E.M. Earley, E. Verschueren, D.L. Swaney, G. Skibinski, J. van Haren, R.J. Nichols, T. Wittmann, S. Finkbeiner, N.J. Krogan, S.A. Oakes, A. Hiniker; Project administration: N.J. Krogan, S.A. Oakes, A. Hiniker; Resources: D.L. Swaney, G. Skibinski, C. Mirescu, C. Iaccarino, W.T. Dauer, R.J. Nichols, T. Wittmann, T.C. Cox, S. Finkbeiner, N.J. Krogan, S.A. Oakes, A. Hiniker; Supervision: G. Skibinski, T. Wittmann, C. Iaccarino, S. Finkbeiner, N.J. Krogan, S.A. Oakes, A. Hiniker; Validation: A.E.D. Stormo, F. Shavarebi, M. FitzGibbon, E.M. Earley, H. Ahrendt, L.S. Lum, A. Hiniker; Visualization: A.E.D. Stormo, E.M. Earley, G. Skibinski, E. Verschueren, J. Van Haren, T. Wittmann, A. Hiniker; Writing - original draft: A.E.D. Stormo, S.A. Oakes, A. Hiniker; Writing - review & editing: A.E.D. Stormo, F. Shaverebi, E. Verschueren, D.L. Swaney, G. Skibinski, T. Wittmann, T.C. Cox, S. Finkbeiner, N.J. Krogan, S.A. Oakes, A. Hiniker.

Submitted: 12 October 2020
Revised: 26 October 2021
Accepted: 4 January 2022

References

Alegre-Abarrategui, J., H. Christian, M.M.P. Lufino, R. Mutihac, L.L. Venda, O. Ansorge, and R. Wade-Martins. 2009. LRRK2 regulates autophagic activity and localizes to specific membrane microdomains in a novel human genomic reporter cellular model. *Hum. Mol. Genet.* 18: 4022–4034. https://doi.org/10.1093/hmg/ddp346

Arrasate, M., S. Mitra, E.S. Schweitzer, M.R. Segal, and S. Finkbeiner. 2004. Inclusion body formation reduces levels of mutant huntingtin and the risk of neuronal death. *Nature*. 431:805–810. https://doi.org/10.1038/nature02998

Barmada, S.J., A. Serio, A. Arjun, B. Bilican, A. Daub, D.M. Ando, A. Tsvetkov, M. Pleiss, X. Li, D. Peisach, C. Shaw, et al. 2014. Autophagy induction enhances TDP43 turnover and survival in neuronal ALS models. *Nat. Chem. Biol.* 10:677–685. https://doi.org/10.1038/nchembio.1563

Beilina, A., I.N. Rudenko, A. Kaganovich, L. Civiero, H. Chau, S.K. Kalia, L.V. Kalia, E. Lobbestael, R. Chia, K. Ndukwe, J. Ding, et al. 2014. Unbiased screen for interactors of leucine-rich repeat kinase 2 supports a common pathway for sporadic and familial Parkinson disease. *Proc. Natl. Acad. Sci. USA*. 111:2626–2631. https://doi.org/10.1073/pnas.1318306111

Brademan, D.R., N.M. Riley, N.W. Kwiecien, and J.J. Coon. 2019. Interactive peptide spectral annotator: a versatile web-based tool for proteomic applications. *Mol. Cell. Proteomics*. 18:S193–S201. https://doi.org/10.1074/mcp.TIR118.001209

Buchner, G., E. Montini, G. Andolfi, N. Quaderi, S. Cainarca, S. Messali, M.T. Bassi, A. Ballabio, G. Meroni, and B. Franco. 1999. MID2, a homologue of the Opitz syndrome gene MID1: similarities in subcellular localization and differences in expression during development. *Hum. Mol. Genet.* 8: 1397–1407. https://doi.org/10.1093/hmg/8.8.1397

Caesar, M., S. Zach, C.B. Carlson, K. Brockmann, T. Gasser, and F. Gillardon. 2013. Leucine-rich repeat kinase 2 functionally interacts with microtubules and kinase-dependently modulates cell migration. *Neurobiol. Dis.* 54:280–288. https://doi.org/10.1016/j.nbd.2012.12.019

Cau, Y., D. Valensin, M. Mori, S. Draghi, and M. Botta. 2018. Structure, function, involvement in diseases and targeting of 14-3-3 proteins: an update. *Curr. Med. Chem.* 25:5–21. https://doi.org/10.2174/0929867324666170426095015

Choi, M., C.Y. Chang, T. Clough, D. Broudy, T. Killeen, B. MacLean, and O. Vitek. 2014. MSstats: an R package for statistical analysis of quantitative mass spectrometry-based proteomic experiments. *Bioinformatics*. 30: 2524–2526. https://doi.org/10.1093/bioinformatics/btu305

Das, K.P., T.M. Freudenrich, and W.R. Mundy. 2004. Assessment of PC12 cell differentiation and neurite growth: a comparison of morphological and neurochemical measures. *Neurotoxicol. Teratol.* 26:397–406. https://doi.org/10.1016/j.ntt.2004.02.006

Davies, P., K.M. Hinkle, N.N. Sukar, B. Sepulveda, R. Mesias, G. Serrano, D.R. Alessi, T.G. Beach, D.L. Benson, C.L. White, R.M. Cowell, et al. 2013. Comprehensive characterization and optimization of anti-LRRK2 (leucine-rich repeat kinase 2) monoclonal antibodies. *Biochem. J.* 453: 101–113. https://doi.org/10.1042/BJ20121742

de Lau, L.M., and M.M.B. Breteler. 2006. Epidemiology of Parkinson's disease. *Lancet Neurol.* 5:525–535. https://doi.org/10.1016/S1474-4422(06)70471-9

Deniston, C.K., J. Salogiannis, S. Mathea, D.M. Snead, I. Lahiri, M. Matyszewski, O. Donosa, R. Watanabe, J. Bohning, A.K. Shiau, S. Knapp, et al. 2020. Structure of LRRK2 in Parkinson's disease and model for microtubule interaction. *Nature*. 588:344–349. https://doi.org/10.1038/s41586-020-2673-2

Dhekne, H.S., I. Yanatori, R.C. Gomez, F. Tonelli, F. Diez, B. Schule, M. Steger, D.R. Alessi, and S.R. Pfeffer. 2018. A pathway for Parkinson's Disease LRRK2 kinase to block primary cilia and Sonic hedgehog signaling in the brain. *Elife*. 7:e40202. https://doi.org/10.7554/eLife.40202

Di Maio, R., E.K. Hoffman, E.M. Rocha, M.T. Keeney, L.H. Sanders, B.R. De Miranda, A. Zharikov, A. Van Laar, A.F. Stepan, T.A. Lanz, J.K. Kofler, et al. 2018. LRRK2 activation in idiopathic Parkinson's disease. *Sci. Transl. Med.* 10:eaar5429. https://doi.org/10.1126/scitranslmed.aar5429

Ding, X., and M.S. Goldberg. 2009. Regulation of LRRK2 stability by the E3 ubiquitin ligase CHIP. *PLoS One*. 4:e5949. https://doi.org/10.1371/journal.pone.0005949

Dzamko, N., M. Deak, F. Hentati, A.D. Reith, A.R. Prescott, D.R. Alessi, and R.J. Nichols. 2010. Inhibition of LRRK2 kinase activity leads to dephosphorylation of Ser(910)/Ser(935), disruption of 14-3-3 binding and altered cytoplasmic localization. *Biochem. J.* 430:405–413. https://doi.org/10.1042/BJ20100784

Edkins, A.L. 2015. CHIP: a co-chaperone for degradation by the proteasome. *Subcell. Biochem.* 78:219–242. https://doi.org/10.1007/978-3-319-11731-7_11

Eguchi, T., T. Kuwahara, M. Sakurai, T. Komori, T. Fujimoto, G. Ito, S.I. Yoshimura, A. Harada, M. Fukuda, M. Koike, and T. Iwatsubo. 2018. LRRK2 and its substrate Rab GTPases are sequentially targeted onto stressed lysosomes and maintain their homeostasis. *Proc. Natl. Acad. Sci. USA*. 115:E9115–E9124. https://doi.org/10.1073/pnas.1812196115

Gandhi, P.N., X. Wang, X. Zhu, S.G. Chen, and A.L. Wilson-Delfosse. 2008. The Roc domain of leucine-rich repeat kinase 2 is sufficient for interaction with microtubules. *J. Neurosci. Res.* 86:1711–1720. https://doi.org/10.1002/jnr.21622

Geetha, T.S., K.A. Michealraj, M. Kabra, G. Kaur, R.C. Juyal, and B.K. Thelma. 2014. Targeted deep resequencing identifies MID2 mutation for X-linked intellectual disability with varied disease severity in a large kindred from India. *Hum. Mutat.* 35:41–44. https://doi.org/10.1002/humu.22453

Gholkar, A.A., S. Senese, Y.C. Lo, E. Vides, E. Contreras, E. Hodara, J. Capri, J.P. Whitelegge, and J.Z. Torres. 2016. The X-linked-intellectual-disability-associated ubiquitin ligase Mid2 interacts with astrin and regulates astrin levels to promote cell division. *Cell Rep.* 14:180–188. https://doi.org/10.1016/j.celrep.2015.12.035

Godena, V.K., N. Brookes-Hocking, A. Moller, G. Shaw, M. Oswald, R.M. Sancho, C.C.J. Miller, A.J. Whitworth, and K.J. De Vos. 2014. Increasing microtubule acetylation rescues axonal transport and locomotor deficits caused by LRRK2 Roc-COR domain mutations. *Nat. Commun.* 5:5245. https://doi.org/10.1038/ncomms6245

Greggio, E., I. Zambrano, A. Kaganovich, A. Beilina, J.M. Taymans, V. Daniels, P. Lewis, S. Jain, J. Ding, A. Syed, K.J. Thomas, et al. 2008. The Parkinson disease-associated leucine-rich repeat kinase 2 (LRRK2) is a dimer that undergoes intramolecular autophosphorylation. *J. Biol. Chem.* 283:16906–16914. https://doi.org/10.1074/jbc.M708718200

Hartlova, A., S. Herbst, J. Peltier, A. Rodgers, O. Bilkei-Gorzo, A. Fearns, B.D. Dill, H. Lee, R. Flynn, S.A. Cowley, P. Davies, et al. 2018. LRRK2 is a negative regulator of Mycobacterium tuberculosis phagosome maturation in macrophages. *EMBO J.* 37:e98694. https://doi.org/10.15252/embj.201798694

Horlbeck, M.A., L.A. Gilbert, J.E. Villalta, B. Adamson, R.A. Pak, Y. Chen, A.P. Fields, C.Y. Park, J.E. Corn, M. Kampmann, and J.S. Weissman. 2016. Compact and highly active next-generation libraries for CRISPR-mediated gene repression and activation. *Elife*. 5:e19760. https://doi.org/10.7554/eLife.19760

Jager, S., P. Cimermancic, N. Gulbahce, J.R. Johnson, K.E. McGovern, S.C. Clarke, M. Shales, G. Mercenne, L. Pache, K. Li, H. Hernandez, et al. 2011. Global landscape of HIV-human protein complexes. *Nature*. 481: 365–370. https://doi.org/10.1038/nature10719

Kalogeropulou, A., J. Freemantle, P. Lis, E. Vides, N. Polinski, and D. Alessi. 2020. Endogenous Rab29 does not impact basal or nigericin and monensin stimulated LRRK2 pathway activity. *bioRxiv*. https://doi.org/10.1101/2020.06.08.139675 (Preprint posted October 7, 2020)

Kett, L.R., D. Boassa, C.C.Y. Ho, H.J. Rideout, J. Hu, M. Terada, M. Ellisman, and W.T. Dauer. 2012. LRRK2 Parkinson disease mutations enhance its microtubule association. *Hum. Mol. Genet.* 21:890–899. https://doi.org/10.1093/hmg/ddr526

Klein, C., and A. Westenberger. 2012. Genetics of Parkinson's disease. *Cold Spring Harb. Perspect. Med.* 2:a008888. https://doi.org/10.1101/cshperspect.a008888

Ko, H.S., R. Bailey, W.W. Smith, Z. Liu, J.H. Shin, Y.I. Lee, Y.J. Zhang, H. Jiang, C.A. Ross, D.J. Moore, C. Patterson, et al. 2009. CHIP regulates leucine-rich repeat kinase-2 ubiquitination, degradation, and toxicity. *Proc. Natl. Acad. Sci. USA*. 106:2897–2902. https://doi.org/10.1073/pnas.0810123106

Kumari, U., and E.K. Tan. 2009. LRRK2 in Parkinson's disease: genetic and clinical studies from patients. *FEBS J.* 276:6455–6463. https://doi.org/10.1111/j.1742-4658.2009.07344.x

Lara Ordonez, A.J., B. Fernandez, E. Fdez, M. Romo-Lozano, J. Madero-Perez, E. Lobbestael, V. Baekelandt, A. Aiastui, A. Lopez de Munain, H.L. Melrose, L. Civiero, et al. 2019. RAB8, RAB10 and RILPL1 contribute to both LRRK2 kinase-mediated centrosomal cohesion and ciliogenesis deficits. *Hum. Mol. Genet.* 28:3552–3568. https://doi.org/10.1093/hmg/ddz201

Larson, M.H., L.A. Gilbert, X. Wang, W.A. Lim, J.S. Weissman, and L.S. Qi. 2013. CRISPR interference (CRISPRi) for sequence-specific control of gene expression. *Nat. Protoc.* 8:2180–2196. https://doi.org/10.1038/nprot.2013.132

Law, B.M.H., V.A. Spain, V.H.L. Leinster, R. Chia, A. Beilina, H.J. Cho, J.M. Taymans, M.K. Urban, R.M. Sancho, M. Blanca Ramirez, S. Biskup, et al. 2014. A direct interaction between leucine-rich repeat kinase 2 and specific beta-tubulin isoforms regulates tubulin acetylation. *J. Biol. Chem.* 289:895–908. https://doi.org/10.1074/jbc.M113.507913

Li, X., Q.J. Wang, N. Pan, S. Lee, Y. Zhao, B.T. Chait, and Z. Yue. 2011. Phosphorylation-dependent 14-3-3 binding to LRRK2 is impaired by common mutations of familial Parkinson's disease. *PLoS One*. 6:e17153. https://doi.org/10.1371/journal.pone.0017153

Liao, J., C.X. Wu, C. Burlak, S. Zhang, H. Sahm, M. Wang, Z.Y. Zhang, K.W. Vogel, M. Federici, S.M. Riddle, R.J. Nichols, et al. 2014. Parkinson disease-associated mutation R1441H in LRRK2 prolongs the "active state" of its GTPase domain. *Proc. Natl. Acad. Sci. USA*. 111:4055–4060. https://doi.org/10.1073/pnas.1323285111

Lim, K.L., K.C. Chew, J.M. Tan, C. Wang, K.K. Chung, Y. Zhang, Y. Tanaka, W. Smith, S. Engelender, C.A. Ross, V.L. Dawson, et al. 2005. Parkin mediates nonclassical, proteasomal-independent ubiquitination of synphilin-1: implications for Lewy body formation. *J. Neurosci.* 25: 2002–2009. https://doi.org/10.1523/jneurosci.4474-04.2005

Liu, Z., J. Lee, S. Krummey, W. Lu, H. Cai, and M.J. Lenardo. 2011. The kinase LRRK2 is a regulator of the transcription factor NFAT that modulates the severity of inflammatory bowel disease. *Nat. Immunol.* 12: 1063–1070. https://doi.org/10.1038/ni.2113

Liu, Z., and M.J. Lenardo. 2012. The role of LRRK2 in inflammatory bowel disease. *Cell Res.* 22:1092–1094. https://doi.org/10.1038/cr.2012.42

Lobbestael, E., L. Civiero, T. De Wit, J.M. Taymans, E. Greggio, and V. Baekelandt. 2016. Pharmacological LRRK2 kinase inhibition induces LRRK2 protein destabilization and proteasomal degradation. *Sci. Rep.* 6:33897. https://doi.org/10.1038/srep33897

MacLeod, D., J. Dowman, R. Hammond, T. Leete, K. Inoue, and A. Abeliovich. 2006. The familial Parkinsonism gene LRRK2 regulates neurite process morphology. *Neuron*. 52:587–593. https://doi.org/10.1016/j.neuron.2006.10.008

Manschwetus, J.T., M. Wallbott, A. Fachinger, C. Obergruber, S. Pautz, D. Bertinetti, S.H. Schmidt, and F.W. Herberg. 2020. Binding of the human

14-3-3 isoforms to distinct sites in the leucine-rich repeat kinase 2. *Front. Neurosci.* 14:302. https://doi.org/10.3389/fnins.2020.00302
McGrath, E., D. Waschbusch, B.M. Baker, and A.R. Khan. 2019. LRRK2 binds to the Rab32 subfamily in a GTP-dependent manner via its armadillo domain. *Small GTPases*. 12:133–146. https://doi.org/10.1080/21541248.2019.1666623
Meroni, G. 2012. Genomics and evolution of the TRIM gene family. *Adv. Exp. Med. Biol.* 770:1–9. https://doi.org/10.1007/978-1-4614-5398-7_1
Migheli, R., M.G. Del Giudice, Y. Spissu, G. Sanna, Y. Xiong, T.M. Dawson, V.L. Dawson, M. Galioto, G. Rocchitta, A. Biosa, P.A. Serra, et al. 2013. LRRK2 affects vesicle trafficking, neurotransmitter extracellular level and membrane receptor localization. *PLoS One*. 8:e77198. https://doi.org/10.1371/journal.pone.0077198
Muda, K., D. Bertinetti, F. Gesellchen, J.S. Hermann, F. von Zweydorf, A. Geerlof, A. Jacob, M. Ueffing, C.J. Gloeckner, and F.W. Herberg. 2014. Parkinson-related LRRK2 mutation R1441C/G/H impairs PKA phosphorylation of LRRK2 and disrupts its interaction with 14-3-3. *Proc. Natl. Acad. Sci. USA*. 111:E34–E43. https://doi.org/10.1073/pnas.1312701111
Myasnikov, A., H. Zhu, P. Hixson, B. Xie, K. Yu, A. Pitre, J. Peng, and J. Sun. 2021. Structural analysis of the full-length human LRRK2. *Cell*. 184:3519–3527.e10. https://doi.org/10.1016/j.cell.2021.05.004.
Nichols, R.J., N. Dzamko, N.A. Morrice, D.G. Campbell, M. Deak, A. Ordureau, T. Macartney, Y. Tong, J. Shen, A.R. Prescott, and D.R. Alessi. 2010. 14-3-3 binding to LRRK2 is disrupted by multiple Parkinson's disease-associated mutations and regulates cytoplasmic localization. *Biochem. J.* 430:393–404. https://doi.org/10.1042/BJ20100483
Nucifora, F.C. Jr., L.G. Nucifora, C.H. Ng, N. Arbez, Y. Guo, E. Roby, V. Shani, S. Engelender, D. Wei, X.F. Wang, T. Li, et al. 2016. Ubiquitination via K27 and K29 chains signals aggregation and neuronal protection of LRRK2 by WSB1. *Nat. Commun.* 7:11792. https://doi.org/10.1038/ncomms11792
Orenstein, S.J., S.H. Kuo, I. Tasset, E. Arias, H. Koga, I. Fernandez-Carasa, E. Cortes, L.S. Honig, W. Dauer, A. Consiglio, A. Raya, et al. 2013. Interplay of LRRK2 with chaperone-mediated autophagy. *Nat. Neurosci.* 16:394–406. https://doi.org/10.1038/nn.3350
Ozelius, L.J., G. Senthil, R. Saunders-Pullman, E. Ohmann, A. Deligtisch, M. Tagliati, A.L. Hunt, C. Klein, B. Henick, S.M. Hailpern, R.B. Lipton, et al. 2006. LRRK2 G2019S as a cause of Parkinson's disease in Ashkenazi Jews. *N. Engl. J. Med.* 354:424–425. https://doi.org/10.1056/NEJMc055509
Pankratz, N., W.C. Nichols, S.K. Uniacke, C. Halter, J. Murrell, A. Rudolph, C.W. Shults, P.M. Conneally, T. Foroud, and Parkinson Study Group. 2003. Genome-wide linkage analysis and evidence of gene-by-gene interactions in a sample of 362 multiplex Parkinson disease families. *Hum. Mol. Genet.* 12:2599–2608. https://doi.org/10.1093/hmg/ddg270
Perry, J., K.M. Short, J.T. Romer, S. Swift, T.C. Cox, and A. Ashworth. 1999. FXY2/MID2, a gene related to the X-linked Opitz syndrome gene FXY/MID1, maps to Xq22 and encodes a FNIII domain-containing protein that associates with microtubules. *Genomics*. 62:385–394. https://doi.org/10.1006/geno.1999.6043
Petrucelli, L., D. Dickson, K. Kehoe, J. Taylor, H. Snyder, A. Grover, M. De Lucia, E. McGowan, J. Lewis, G. Prihar, J. Kim, et al. 2004. CHIP and Hsp70 regulate tau ubiquitination, degradation and aggregation. *Hum. Mol. Genet.* 13:703–714. https://doi.org/10.1093/hmg/ddh083
Plowey, E.D., S.J. Cherra 3rd, Y.J. Liu, and C.T. Chu. 2008. Role of autophagy in G2019S-LRRK2-associated neurite shortening in differentiated SH-SY5Y cells. *J. Neurochem.* 105:1048–1056. https://doi.org/10.1111/j.1471-4159.2008.05217.x
Purlyte, E., H.S. Dhekne, A.R. Sarhan, R. Gomez, P. Lis, M. Wightman, T.N. Martinez, F. Tonelli, S.R. Pfeffer, and D.R. Alessi. 2018. Rab29 activation of the Parkinson's disease-associated LRRK2 kinase. *EMBO J.* 37:1–18. https://doi.org/10.15252/embj.201798099
Rajalingam, K., and I. Dikic. 2016. SnapShot: expanding the ubiquitin code. *Cell*. 164:1074–1074.e1. https://doi.org/10.1016/j.cell.2016.02.019..
Rajsbaum, R., J.P. Stoye, and A. O'Garra. 2008. Type I interferon-dependent and -independent expression of tripartite motif proteins in immune cells. *Eur. J. Immunol.* 38:619–630. https://doi.org/10.1002/eji.200737916
Ran, F.A., P.D. Hsu, J. Wright, V. Agarwala, D.A. Scott, and F. Zhang. 2013. Genome engineering using the CRISPR-Cas9 system. *Nat. Protoc.* 8:2281–2308. https://doi.org/10.1038/nprot.2013.143
Reyniers, L., M.G. Del Giudice, L. Civiero, E. Belluzzi, E. Lobbestael, A. Beilina, G. Arrigoni, R. Derua, E. Waelkens, Y. Li, C. Crosio, et al. 2014. Differential protein-protein interactions of LRRK1 and LRRK2 indicate roles in distinct cellular signaling pathways. *J. Neurochem.* 131:239–250. https://doi.org/10.1111/jnc.12798
Rudenko, I.N., and M.R. Cookson. 2010. 14-3-3 proteins are promising LRRK2 interactors. *Biochem. J.* 430:e5–6. https://doi.org/10.1042/BJ20101200..
Rudenko, I.N., A. Kaganovich, R.G. Langston, A. Beilina, K. Ndukwe, R. Kumaran, A.A. Dillman, R. Chia, and M.R. Cookson. 2017. The G2385R risk factor for Parkinson's disease enhances CHIP-dependent intracellular degradation of LRRK2. *Biochem. J.* 474:1547–1558. https://doi.org/10.1042/BCJ20160909
Salasova, A., C. Yokota, D. Potesil, Z. Zdrahal, V. Bryja, and E. Arenas. 2017. A proteomic analysis of LRRK2 binding partners reveals interactions with multiple signaling components of the WNT/PCP pathway. *Mol. Neurodegener.* 12:54. https://doi.org/10.1186/s13024-017-0193-9
Schmidt, S.H., M.J. Knape, D. Boassa, N. Mumdey, A.P. Kornev, M.H. Ellisman, S.S. Taylor, and F.W. Herberg. 2019. The dynamic switch mechanism that leads to activation of LRRK2 is embedded in the DFGpsi motif in the kinase domain. *Proc. Natl. Acad. Sci. USA*. 116:14979–14988. https://doi.org/10.1073/pnas.1900289116
Sejwal, K., M. Chami, H. Remigy, R. Vancraenenbroeck, W. Sibran, R. Sutterlin, P. Baumgartner, R. McLeod, M.C. Chartier-Harlin, V. Baekelandt, H. Stahlberg, et al. 2017. Cryo-EM analysis of homodimeric full-length LRRK2 and LRRK1 protein complexes. *Sci. Rep.* 7:8667. https://doi.org/10.1038/s41598-017-09126-z
Shaner, N.C., R.E. Campbell, P.A. Steinbach, B. N. G. Giepmans, A.E. Palmer, and R.Y. Tsien. 2004. Improved monomeric red, orange and yellow fluorescent proteins derived from Discosoma sp. red fluorescent protein. *Nat. Biotechnol.* 22:1567–1572. https://doi.org/10.1038/nbt1037
Sheng, Z., S. Zhang, D. Bustos, T. Kleinheinz, C.E. Le Pichon, S.L. Dominguez, H.O. Solanoy, J. Drummond, X. Zhang, X. Ding, F. Cai, et al. 2012. Ser1292 autophosphorylation is an indicator of LRRK2 kinase activity and contributes to the cellular effects of PD mutations. *Sci. Transl. Med.* 4:164ra161. https://doi.org/10.1126/scitranslmed.3004485
Short, K.M., and T.C. Cox. 2006. Subclassification of the RBCC/TRIM superfamily reveals a novel motif necessary for microtubule binding. *J. Biol. Chem.* 281:8970–8980. https://doi.org/10.1074/jbc.M512755200
Short, K.M., B. Hopwood, Z. Yi, and T.C. Cox. 2002. MID1 and MID2 homo- and heterodimerise to tether the rapamycin-sensitive PP2A regulatory subunit, alpha 4, to microtubules: implications for the clinical variability of X-linked Opitz GBBB syndrome and other developmental disorders. *BMC Cell Biol.* 3:1. https://doi.org/10.1186/1471-2121-3-1
Skibinski, G., V. Hwang, D.M. Ando, A. Daub, A.K. Lee, A. Ravisankar, S. Modan, M.M. Finucane, B.A. Shaby, and S. Finkbeiner. 2017. Nrf2 mitigates LRRK2- and alpha-synuclein-induced neurodegeneration by modulating proteostasis. *Proc. Natl. Acad. Sci. USA*. 114:1165–1170. https://doi.org/10.1073/pnas.1522872114
Skibinski, G., K. Nakamura, M.R. Cookson, and S. Finkbeiner. 2014. Mutant LRRK2 toxicity in neurons depends on LRRK2 levels and synuclein but not kinase activity or inclusion bodies. *J. Neurosci.* 34:418–433. https://doi.org/10.1523/jneurosci.2712-13.2014
Steger, M., F. Diez, H.S. Dhekne, P. Lis, R.S. Nirujogi, O. Karayel, F. Tonelli, T.N. Martinez, E. Lorentzen, S.R. Pfeffer, D.R. Alessi, et al. 2017. Systematic proteomic analysis of LRRK2-mediated Rab GTPase phosphorylation establishes a connection to ciliogenesis. *Elife*. 6:e31012. https://doi.org/10.7554/eLife.31012
Steger, M., F. Tonelli, G. Ito, P. Davies, M. Trost, M. Vetter, S. Wachter, E. Lorentzen, G. Duddy, S. Wilson, M.A. Baptista, et al. 2016. Phosphoproteomics reveals that Parkinson's disease kinase LRRK2 regulates a subset of Rab GTPases. *Elife*. 5:e12813. https://doi.org/10.7554/eLife.12813
Stehbens, S.J., M. Paszek, H. Pemble, A. Ettinger, S. Gierke, and T. Wittmann. 2014. CLASPs link focal-adhesion-associated microtubule capture to localized exocytosis and adhesion site turnover. *Nat. Cell Biol.* 16:561–573. https://doi.org/10.1038/ncb2975
Tanji, K., T. Kamitani, F. Mori, A. Kakita, H. Takahashi, and K. Wakabayashi. 2010. TRIM9, a novel brain-specific E3 ubiquitin ligase, is repressed in the brain of Parkinson's disease and dementia with Lewy bodies. *Neurobiol. Dis.* 38:210–218. https://doi.org/10.1016/j.nbd.2010.01.007
Taylor, M., and D.R. Alessi. 2020. Advances in elucidating the function of leucine-rich repeat protein kinase-2 in normal cells and Parkinson's disease. *Curr. Opin. Cell Biol.* 63:102–113. https://doi.org/10.1016/j.ceb.2020.01.001
Trockenbacher, A., V. Suckow, J. Foerster, J. Winter, S. Krauss, H.H. Ropers, R. Schneider, and S. Schweiger. 2001. MID1, mutated in Opitz syndrome, encodes an ubiquitin ligase that targets phosphatase 2A for degradation. *Nat. Genet.* 29:287–294. https://doi.org/10.1038/ng762
Tsvetkov, A.S., M. Arrasate, S. Barmada, D.M. Ando, P. Sharma, B.A. Shaby, and S. Finkbeiner. 2013. Proteostasis of polyglutamine varies among

neurons and predicts neurodegeneration. *Nat. Chem. Biol.* 9:586–592. https://doi.org/10.1038/nchembio.1308

Watanabe, R., R. Buschauer, J. Bohning, M. Audagnotto, K. Lasker, T.W. Lu, D. Boassa, S. Taylor, and E. Villa. 2020. The in situ structure of Parkinson's disease-linked LRRK2. *Cell.* 182:1508–1518.e16. https://doi.org/10.1016/j.cell.2020.08.004

Wu, C.X., J. Liao, Y. Park, X. Reed, V.A. Engel, N.C. Hoang, Y. Takagi, S.M. Johnson, M. Wang, M. Federici, R.J. Nichols, et al. 2019. Parkinson's disease-associated mutations in the GTPase domain of LRRK2 impair its nucleotide-dependent conformational dynamics. *J. Biol. Chem.* 294:5907–5913. https://doi.org/10.1074/jbc.RA119.007631

Zhang, F.R., W. Huang, S.M. Chen, L.D. Sun, H. Liu, Y. Li, Y. Cui, X.X. Yan, H.T. Yang, R.D. Yang, T.S. Chu, et al. 2009. Genomewide association study of leprosy. *N. Engl. J. Med.* 361:2609–2618. https://doi.org/10.1056/NEJMoa0903753

Zhao, J., T.P. Molitor, J.W. Langston, and R.J. Nichols. 2015. LRRK2 dephosphorylation increases its ubiquitination. *Biochem. J.* 469:107–120. https://doi.org/10.1042/BJ20141305

JCB

Supplemental material

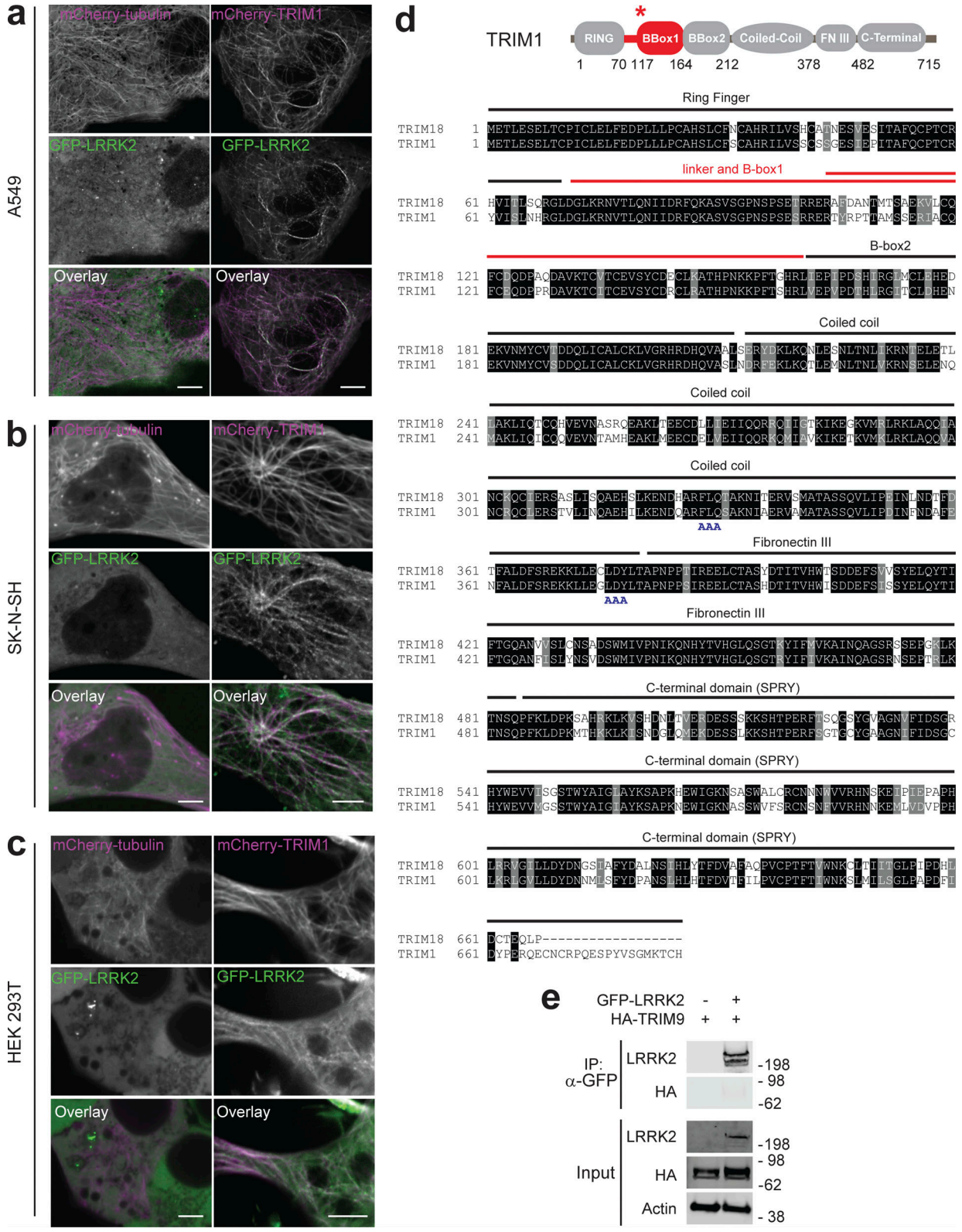

Figure S1. **Additional characterization of the LRRK2-TRIM1 interaction. (a–c)** Live-cell confocal microscopy of GFP-LRRK2 and mCherry-tubulin or mCherry-TRIM1 transiently transfected into A549 cells (scale bar = 10 µM; a), SK-N-SH cells (scale bar = 5 µM; b) or HEK-293T cells (scale bar = 5 µM; c). From top to bottom, each set shows mCherry-tubulin or mCherry-TRIM1, GFP-LRRK2, merged image. In all lines examined, in the presence of mCherry-tubulin, GFP-LRRK2 is diffusely cytoplasmic, but microtubule-localized in the presence of mCherry-TRIM1. **(d)** Alignment of TRIM18 with TRIM1. Domains labeled above alignment. Red line designates region required for TRIM1 interaction with LRRK2. Double red line designates region of least homology in TRIM1 and TRIM18 dual B-box domain. Dual-AAA motifs below the sequence designate the mutated amino acids used to make cytoplasmic TRIM1 C variant. **(e)** Immunoprecipitation of GFP-LRRK2, which fails to coimmunoprecipitate with HA-TRIM9 in HEK-293T cells. Source data are available for this figure: SourceData FS1.

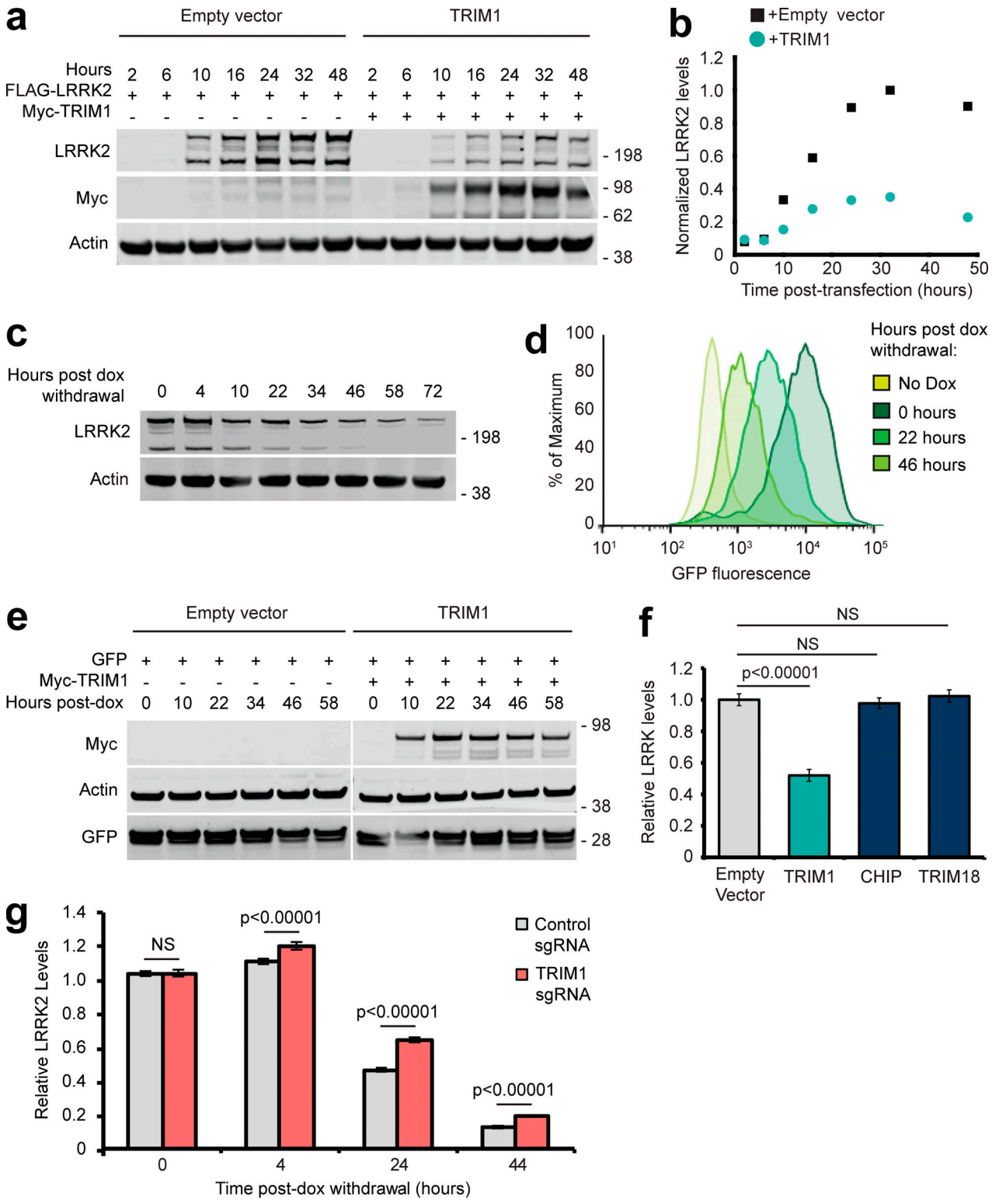

Figure S2. **Evaluation of LRRK2 levels and validation of flow cytometric system to measure LRRK2 turnover. (a)** Immunoblot of FLAG-LRRK2 co-transfected with myc-TRIM1 or empty vector control. Time indicates hours after transfection. **(b)** Quantification of panel a with LRRK2 levels normalized to actin. **(c)** Immunoblot showing LRRK2 levels relative to actin after withdrawal of dox (dox-induced for 18 h). **(d)** Histograms of GFP fluorescence from samples immunoblotted in panel c. **(e)** Immunoblot of dox-induced GFP expression cotransfected with myc-TRIM1 or empty vector control. Time indicates hours after transfection. **(f)** Flow cytometric quantification of GFP-LRRK2 levels in the presence of TRIM1, CHIP, or TRIM18. Bars show median green fluorescence intensity, with error bars showing twice the SEM. **(g)** Flow cytometric quantification of GFP-LRRK2 levels in TRIM1 knockdown and control dCas9/dox-GFP-LRRK2 HEK-293T lines 0, 4, 24, and 44 h after dox withdrawal relative to 0 h. Bars show median green fluorescence intensity, with error bars showing twice the SEM. Significance testing for f and g was performed using ANOVA with post hoc *t* test with Bonferroni correction. Source data are available for this figure: SourceData FS2.

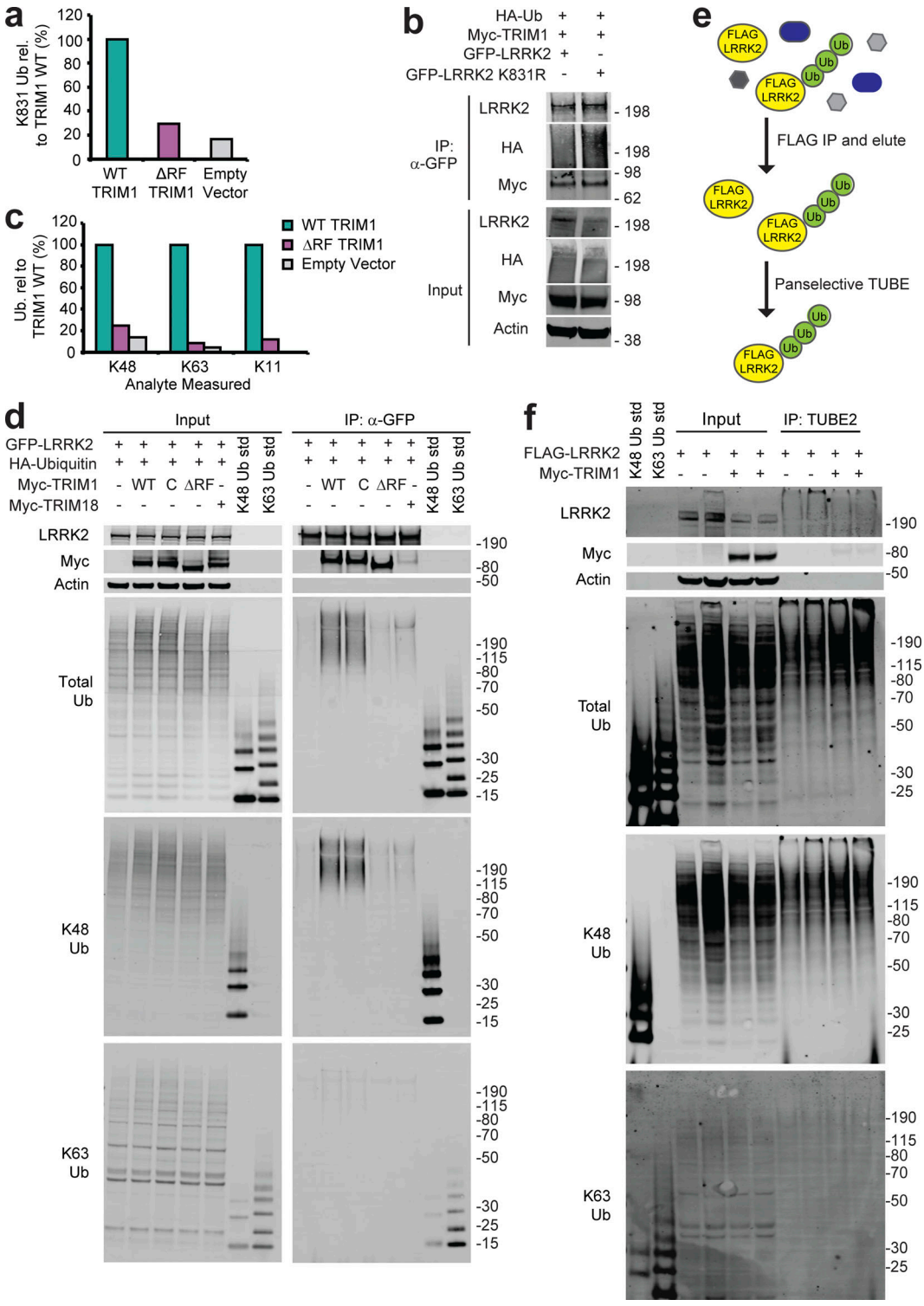

Figure S3. **LRRK2 ubiquitination by TRIM1. (a)** Quantitative MS analysis of LRRK2 K831 ubiquitination (Ub) in the presence of WT TRIM1, ΔRF TRIM1, or empty vector. ("rel." designates relative). **(b)** Coimmunoprecipitation and ubiquitination of GFP-LRRK2 WT or K831R with myc-TRIM1 in the presence of HA-ubiquitin in HEK-293T cells. **(c)** All ubiquitin linkages identified by MS analysis of ubiquitinated LRRK2 eluate in the presence of WT TRIM1, ΔRF TRIM1, or empty vector. **(d)** Coimmunoprecipitation and ubiquitination of GFP-LRRK2 in the presence of HA-ubiquitin and TRIM1 WT, C, or ΔRF or TRIM18 followed by immunoblotting against total ubiquitin, K48-linked ubiquitin, or K63-linked ubiquitin. The immunoblot membrane for the input samples was physically cut to separate the LRRK2-, myc-, and actin-blotted portions, with all regions additionally probed with a primary antibody for total ubiquitin. **(e)** Schematic of TUBE assay. LRRK2 was immunoprecipitated from HEK-293T lysate with anti-FLAG–conjugated agarose resin, and a panselective TUBE was used to isolate ubiquitinated LRRK2, which was analyzed by immunoblot. **(f)** TUBE assay with FLAG-LRRK2 expressed in the presence of myc-TRIM1 or a control vector. TUBE eluates were blotted with broad anti-ubiquitin antibodies as well as K48 and K63 linkage-specific antibodies. All immunoblots are representative of at least three independent experiments. Source data are available for this figure: SourceData FS3.

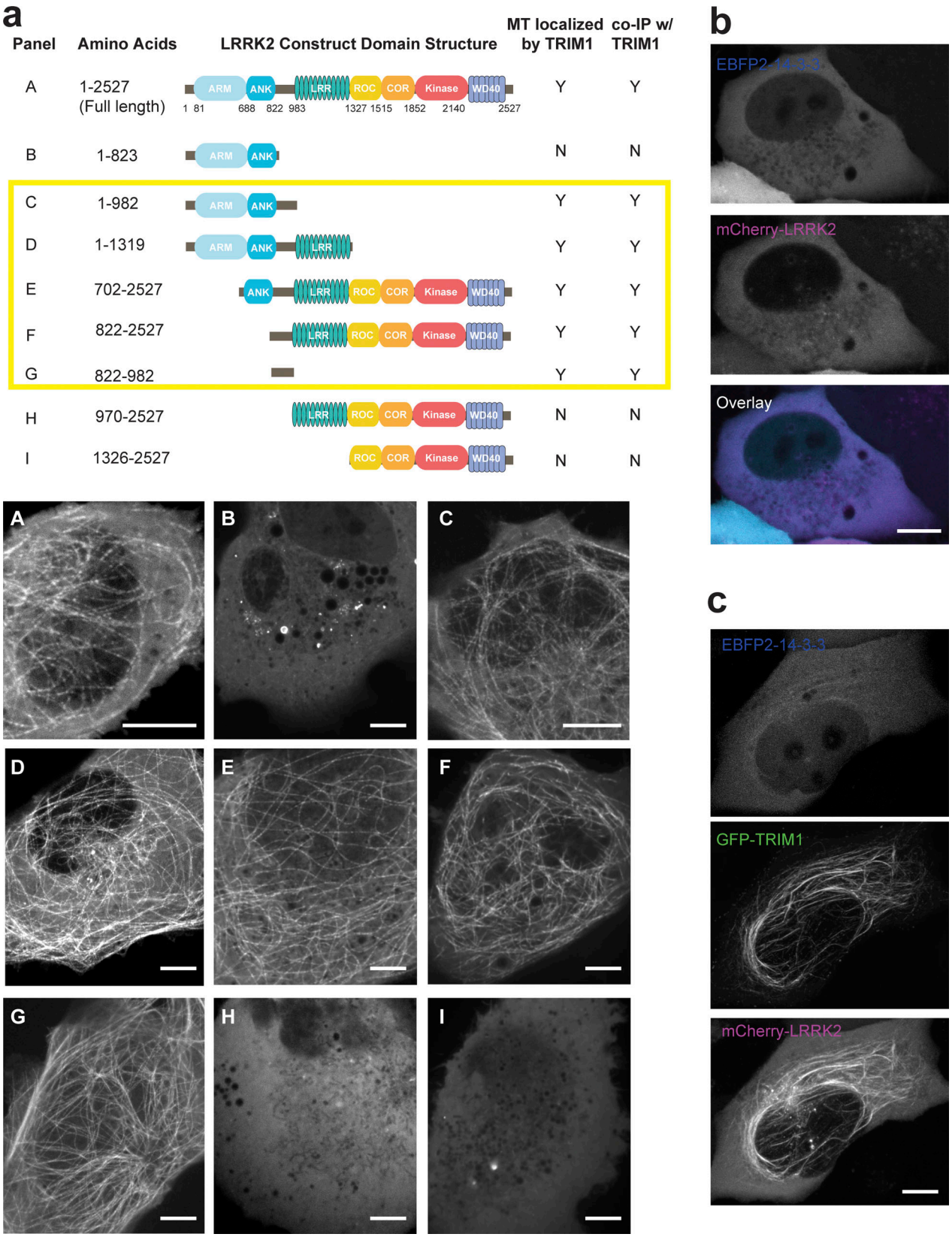

Figure S4. **TRIM1 binds LRRK2-RL to cause LRRK2 microtubule localization. (a)** Schematic of GFP-LRRK2 constructs (above) with corresponding live-cell microscopy in the presence of mCherry-TRIM1 in H1299 cells (below). Each panel shows only fluorescence at 488 nm (GFP) to illustrate the subcellular localization of each GFP-LRRK2 construct in the presence of mCherry-TRIM1, which is always localized to the microtubule network. MT, microtubule. **(b)** Live-cell confocal microscopy of mCherry-LRRK2 in the presence of EBFP2-14-3-3 in H1299 cells. **(c)** Live-cell confocal microscopy of mCherry-LRRK2 in the presence of EBFP2-14-3-3 and GFP-TRIM1 showing individual EBFP2, GFP, and mCherry channels from Fig. 6 a. In all panels, scale bar = 10 µM..

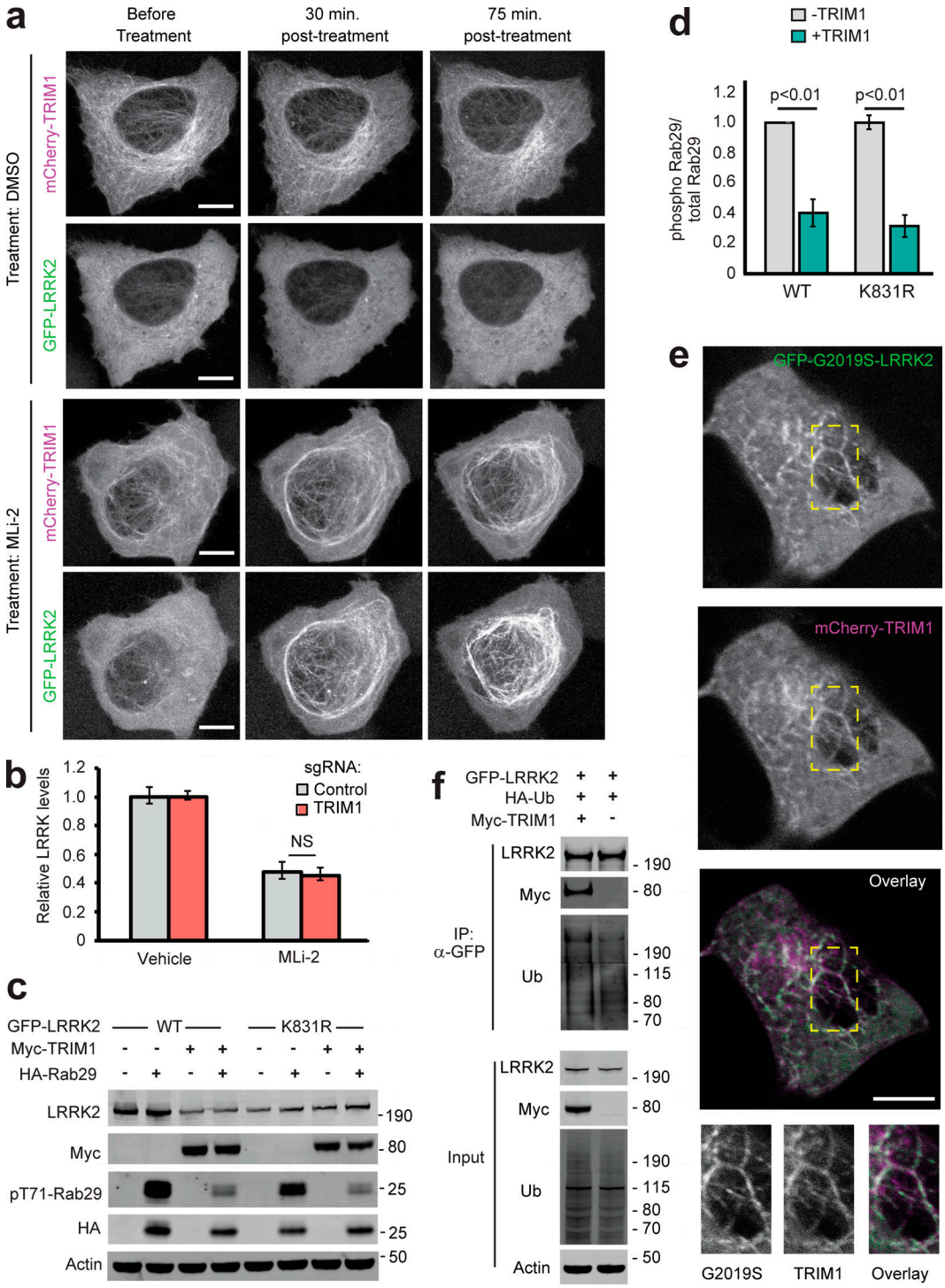

Figure S5. **Additional characterization of effect of TRIM1 on LRRK2 localization and function. (a)** Live-cell confocal microscopy of GFP-LRRK2 in the presence of mCherry-TRIM1 after treatment with LRRK2 kinase inhibitor MLi-2 (200 nM) or vehicle, showing the individual mCherry and GFP channels from the time course in Fig. 6 g. Rare cells with low levels of colocalization before treatment were followed over time. Scale bar = 10 µM. **(b)** Quantification of GFP-LRRK2 fluorescence in flow cytometric assay with TRIM1 knocked down (red bar) compared with cells with nontargeting sgRNA (gray bar). Cells were dox-induced for 24 h, dox was removed, and MLi-2 (100 nM) or vehicle was added for another 24 h before cells were assayed. Bars show median green fluorescence intensity, with error bars showing twice the SEM. **(c)** Immunoblot of Rab29 phosphorylation in the presence and absence of TRIM1 for WT LRRK2 and LRRK2 K831R. **(d)** Quantification of Rab29 phosphorylation in panel c. **(e)** Live-cell confocal microscopy of GFP-LRRK2 G2019S and mCherry-TRIM1 transiently transfected into PC-12 cells (scale bar = 5 µM). From top to bottom: GFP-LRRK2 G2019S, mCherry-TRIM1, merged image, and higher magnification of area in yellow boxes. **(f)** Immunoprecipitation and ubiquitination of GFP-LRRK2 with myc-TRIM1 in the presence of HA-ubiquitin in PC12 cells. The immunoblot membrane was physically cut between LRRK2- and myc-blotted portions, with both sections additionally probed with an anti-ubiquitin primary antibody. Significance testing for panel b was performed using ANOVA with post hoc *t* test with Bonferroni correction, and for panel d, using Mann–Whitney *U* test. Source data are available for this figure: SourceData FS5.

Video 1. **Related to Fig. 2.** Time-lapse of GFP-LRRK2 localization in the presence of mCherry-TRIM1. Frame rate is 15 frames/second.

Provided online are Table S1 and Table S2. Table S1 is related to Fig. 1 and lists LRRK2 interacting partners. Table S2 is related to Fig. 3 and lists LRRK2 peptides and ubiquitination sites identified.